Characterization of a commercial bioluminescence tomography-guided system for pre-clinical radiation research

Xu, Xiangkun; Deng, Zijian; Sforza, Daniel; Tong, Zhishen; Tseng, Yu-Pei; Newman, Ciara; Reinhart, Merle; Tsouchlos, Paul; Devling, Tim; Dehghani, Hamid; Iordachita, Iulian; Wong, John W.; Wang, Ken Kang-Hsin

DOI:
10.1002/mp.16669

Received: 1 December 2022 | Revised: 6 June 2023 | Accepted: 18 July 2023

DOI: 10.1002/mp.16669

RESEARCH ARTICLE

MEDICAL PHYSICS

Characterization of a commercial bioluminescence tomography-guided system for pre-clinical radiation research

Xiangkun Xu[1] | **Zijian Deng**[1] | **Daniel Sforza**[2] | **Zhishen Tong**[1] | **Yu-Pei Tseng**[1] | **Ciara Newman**[1] | **Merle Reinhart**[3] | **Paul Tsouchlos**[3] | **Tim Devling**[3] | **Hamid Dehghani**[4] | **Iulian Iordachita**[5] | **John W. Wong**[2] | **Ken Kang-Hsin Wang**[1]

[1]Biomedical Imaging and Radiation Technology Laboratory (BIRTLab), Department of Radiation Oncology, University of Texas Southwestern Medical Center, Dallas, Texas, USA

[2]Department of Radiation Oncology and Molecular Radiation Sciences, Johns Hopkins University, Baltimore, Maryland, USA

[3]Xstrahl Inc., Suwanee, Georgia, USA

[4]School of Computer Science, University of Birmingham, Birmingham, UK

[5]Laboratory for Computational Sensing and Robotics, Johns Hopkins University, Baltimore, Maryland, USA

Correspondence
Xiangkun Xu and Ken Kang-Hsin Wang, Department of Radiation Oncology, University of Texas Southwestern Medical Center, 2201 Inwood Road, Rm NC8.202, Dallas, TX 75390, USA.
Email: xiangkun.xu@utsouthwestern.edu and kang-hsin.wang@utsouthwestern.edu

Funding information
National Cancer Institute, National Institutes of Health, Grant/Award Numbers: R21CA223403, R37CA230341, R01CA240811; Cancer Prevention and Research Institute of Texas, Grant/Award Numbers: RR200042, RP180770

Abstract

Background: Widely used Cone-beam computed tomography (CBCT)-guided irradiators have limitations in localizing soft tissue targets growing in a low-contrast environment. This hinders small animal irradiators achieving precise focal irradiation.

Purpose: To advance image-guidance for soft tissue targeting, we developed a commercial-grade bioluminescence tomography-guided system (BLT, MuriGlo) for pre-clinical radiation research. We characterized the system performance and demonstrated its capability in target localization. We expect this study can provide a comprehensive guideline for the community in utilizing the BLT system for radiation studies.

Methods: MuriGlo consists of four mirrors, filters, lens, and charge-coupled device (CCD) camera, enabling a compact imaging platform and multi-projection and multi-spectral BLT. A newly developed mouse bed allows animals imaged in MuriGlo and transferred to a small animal radiation research platform (SARRP) for CBCT imaging and BLT-guided irradiation. Methods and tools were developed to evaluate the CCD response linearity, minimal detectable signal, focusing, spatial resolution, distortion, and uniformity. A transparent polycarbonate plate covering the middle of the mouse bed was used to support and image animals from underneath the bed. We investigated its effect on 2D Bioluminescence images and 3D BLT reconstruction accuracy, and studied its dosimetric impact along with the rest of mouse bed. A method based on pinhole camera model was developed to map multi-projection bioluminescence images to the object surface generated from CBCT image. The mapped bioluminescence images were used as the input data for the optical reconstruction. To account for free space light propagation from object surface to optical detector, a spectral derivative (SD) method was implemented for BLT reconstruction. We assessed the use of the SD data (ratio imaging of adjacent wavelength) in mitigating out of focusing and non-uniformity seen in the images. A mouse phantom was used to validate the data mapping. The phantom and an in vivo glioblastoma model were utilized to demonstrate the accuracy of the BLT target localization.

Results: The CCD response shows good linearity with < 0.6% residual from a linear fit. The minimal detectable level is 972 counts for 10 × 10 binning. The focal plane position is within the range of 13–18 mm above the mouse bed. The spatial resolution of 2D optical imaging is < 0.3 mm at Rayleigh criterion. Within the region of interest, the image uniformity is within 5% variation, and image shift due to distortion is within 0.3 mm. The transparent plate caused < 6% light attenuation. The use of the SD imaging data can effectively mitigate out of focusing, image non-uniformity, and the plate attenuation, to support accurate multi-spectral BLT reconstruction. There is < 0.5% attenuation on dose delivery caused by the bed. The accuracy of data mapping from the 2D bioluminescence images to CBCT image is within 0.7 mm. Our phantom test shows the BLT system can localize a bioluminescent target within 1 mm with an optimal threshold and only 0.2 mm deviation was observed for the case with and without a transparent plate. The same localization accuracy can be maintained for the in vivo GBM model.

Conclusions: This work is the first systematic study in characterizing the commercial BLT-guided system. The information and methods developed will be useful for the community to utilize the imaging system for image-guided radiation research.

KEYWORDS

bioluminescence tomography, image-guidance, pre-clinical research, radiation therapy, small animal irradiator

1 | INTRODUCTION

Preclinical radiotherapy (RT) research using small animal models is essential for bridging the gap between in vitro concepts and clinical translation.[1] Imaging-guided technologies are imperative to localize target/tumor and guide irradiation, enabling precise RT studies. Computed tomography (CT) or cone-beam CT (CBCT)-guided small animal irradiators have advanced preclinical research.[2–8] However, it is challenging to guide irradiation for soft tissue targets since CT/CBCT are limited by image contrast, which hinders the irradiators in achieving high-precision delivery and therefore affects study reproducibility.

Bioluminescence imaging (BLI) has been used extensively to monitor tumor growth and response to treatment in animal models by detecting light produced from tumor cells tagged with bioluminescent reporters.[9–11] BLI provides strong image contrast, and thus offers an attractive solution for soft tissue targeting. However, commonly used two-dimensional (2D) BLI on an animal surface is inadequate in providing accurate three-dimensional (3D) localization for radiation guidance. This is because light intensity and distribution are nonlinearly dependent on not only the location of internal bioluminescent target but also tissue optical properties, irregular animal shape, and angles of imaging view to animal surface.[12,13] To overcome these limitations, we and others have incorporated bioluminescence tomography (BLT) with small animal irradiators to guide focal irradiation.[12,14,15] Using an optimization algorithm along with a light propagation model in tissue, we can use BLT to reconstruct the spatially resolved photon emission density of a luminescent tumor by minimizing the difference between the calculated and measured surface bioluminescence signal. With the reconstructed 3D bioluminescent tumor information, BLT has been used to guide irradiation for the orthotopic brain,[15,16] breast,[17] and prostate[14] model, and to monitor tumor response.[17]

To translate our laboratorial-developed optical system[15,18] and its know-how to radiation research community, we collaborated with our industrial partner Xstrahl Inc. and established a compact BLI/BLT system, MuriGlo. MuriGlo was designed to maximize the input for tomographic reconstruction by alleviating the underdetermined nature of BLT through multi-projection imaging using a rotary three-mirror system and multi-spectral imaging using a filter wheel. Compared to our in-house system,[18] an additional fourth mirror was implemented to achieve a compact imaging platform. The BLT system can be integrated with a small animal irradiator via a transportable mouse bed that allows the imaged animal to be transferred between these two systems. The standalone design of the optical system with the transportable bed minimizes the need of modifying existing commercial irradiators and ensures BLI-only applications without occupying the irradiator that affects its experiment throughputs. We also further upgraded the bed originally from the manufacturer; the newly developed mouse bed with a transparent supporting plate allows 360° optical imaging around animal in MuriGlo and easy transfer to a small animal irradiator for CBCT imaging and BLT-guided irradiation. The CBCT imaging not only provides animal anatomical

information but also the coordinate for radiation delivery. In our BLT-guided RT workflow,[18] it is necessary to map surface BLI data to the surface of the animal CBCT image, and the mapped BLI data are used as the input for BLT reconstruction. The resulted BLT reconstructed target defined in the CBCT coordinate can then be utilized for radiation guidance.

In this study, we systematically characterize the performance of the MuriGlo system including 2D BLI and 3D BLT. We designed phantoms and methods to characterize the important metrics for 2D BLI, including charge-coupled device (CCD) response linearity, background and minimum detectable level, and focusing, spatial resolution, distortion, and uniformity. The performance of the multi-spectral BLI, important for BLT reconstruction,[19,20] was investigated; the spectral derivative (SD) data (ratio imaging of adjacent wavelength) was compared to traditional spectral data to examine its effect in mitigating out of focusing and non-uniformity seen in optical images. In regard to 3D BLT, an advanced image registration method, compared to our previous publication,[18] was developed to map multi-projection 2D BLI data to the surface of a 3D numerical mesh generated from an animal CBCT image, used as the input data for the BLT reconstruction. Since a transparent plate was used to support the mouse on the bed and to allow imaging from the bottom of the bed, the effects of the plate on bioluminescence attenuation and BLT target localization were also assessed. Furthermore, we investigated the dosimetric impact of the bed while radiation beams passed through it. We demonstrated the BLT localization accuracy using a mouse phantom inserted with a light source for both SD and non-SD approaches and validated the target localization using an orthotopic bioluminescent glioblastoma (GBM) model.

With the increasing interest of applying BLI/BLT as an image-guided system for radiation research,[15,17,21,22] we expect that the methods and results presented in this work will not only support the use of MuriGlo across institutes, but also provide an insight for the interested investigators in implementing the BLT for accurate image-guided radiation research.

2 | MATERIALS AND METHODS

2.1 | System configuration

MuriGlo was designed with a removable mouse bed and a light-tight chamber. The newly developed mouse bed from our group includes a bed adaptor and a detachable bed, allowing the animal to be imaged in MuriGlo and then readily transferred to the irradiator (Figure 1a). After optical imaging, users can detach the bed from the adaptor along with the imaged animal under anesthesia, and dock the bed to the second adapter placed in the small animal radiation research platform (SARRP; Xstrahl Inc, Suwanee, Georgia, USA), shown in Figure 1a, for subsequent CBCT imaging and irradiation. The rationale of having two identical adaptors, one used in the MuriGlo, and the other one used in the irradiator, is for user convenience and increased throughput. With this design, users can simply dock the mouse bed into the adaptor placed in the SARRP instead of attaching the entire bed and adaptor into the irradiator bed support for each experiment.

Inside the chamber, there is an optical assembly and an added-on thermostatic system developed in-house. The optical assembly consists of a rotary three-mirror system, a fixed mirror (all with 98% reflectivity), filter wheel (Edmund Optics Inc., Barrington, New Jersey, USA), lens (50 mm, f/1.2, Nikkor, Nikon Inc., Melville, New York, USA), and CCD camera (iKon-M934, Andor Technology, Belfast, UK). The optical signal emitted from the imaged object was guided by the three-mirror system and the fixed 45° mirror to the filter wheel, and captured by the CCD camera (Figure 1b). The three-mirror system can rotate 360° around the imaged object for multi-projection imaging. Four 20 nm full-width at half maximum band-pass filters (Chroma Technology Corp., Bellows Falls, Vermont, USA) at 590, 610, 630 and 650 nm were inserted into the filter wheel for multi-spectral imaging. Four light emitting diodes (LED; WS2812B 5050 RGB, Adafruit Industries LLC, New York, New York, USA) were mounted to the three-mirror system to provide white light illumination for photo imaging (Figure 1b). A focus lock was designed in-house and installed to fix the focus ring of the lens to maintain consistent focusing distance to imaged objects.

The thermostatic system was designed in-house to maintain the imaging chamber temperature at desired levels. The system is composed of a type T thermocouple (5TC-GG-T-30-36, Omega, Norwalk, Connecticut, USA), a proportion integration differentiation controller (PID, CN32Pt, Platinum Series, Omega, Norwalk, Connecticut, USA), a solid state relay (SSRL240AC10, Omega, Norwalk, Connecticut, USA), a 24 V transformer, a heater-fan combo (Figure 1b; FCH-FGC15132R, Omega, Norwalk, Connecticut, USA), two circulation fans (Figure S1; CFM-6015V-254-362-20, Digi-Key Electronics, Thief River Falls, Minnesota, USA), a switch with fuse, and two power distribution boards (PCB007; Evemodel, China). Two additional cooling fans (Figure S1; 3610SB-05W-B30-B00, Digi-Key Electronics, Thief River Falls, Minnesota, USA) were installed on the interior MuriGlo cover to circulate air and support CCD operation under −80°C.

The details of the detachable mouse bed docked on the adaptor are shown in Figure 1c. The mouse bed center is made with a transparent plate (polycarbonate, 1.12 mm thick) to support the imaged object and optical image acquisition from the bottom of the bed. The tabs and rubber bands are used to immobilize the imaged

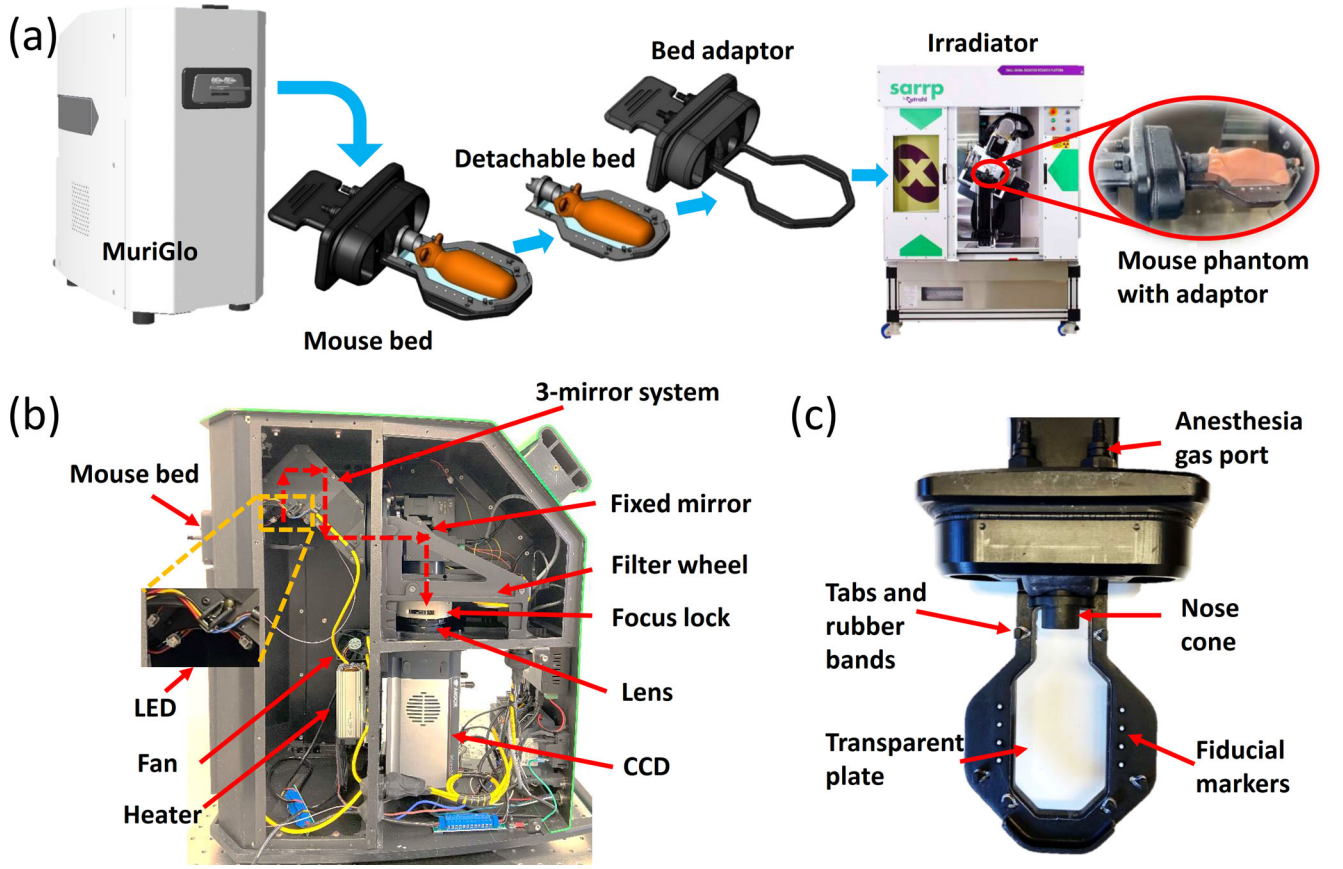

FIGURE 1 (a) shows the workflow of bioluminescence tomography-guided irradiation with MuriGlo in conjunction with a detachable mouse bed, which can be removed from the bed adaptor after optical imaging and docked to the second adaptor placed in an irradiator for CBCT imaging and irradiation. (b) shows MuriGlo configuration and (c) illustrates the detail of the mouse bed and adaptor. CBCT, cone-beam computed tomography. LED, light emitting diode. CCD, charge-coupled device.

animal. The fiducial markers are used for geometric registration between optical and CBCT images. The adaptor is equipped with a nose cone and anesthesia gas port.

2.2 | CCD response linearity

It is important to characterize the linearity of the optical detector, CCD, in response to incident light, particularly for quantitative optical imaging. A cylindrical self-illuminated light source (2 mm in diameter and 6 mm in length, Trigalight, mb-microtec ag, Niederwangen, Switzerland) was inserted into a mouse phantom (XFM-2, Perkin Elmer Inc., Waltham, Massachusetts, USA). The surface images of the phantom were acquired under exposure time from 0.1 to 180 s with 650 nm filter at 1×1 binning, 4× pre-amplifier, and 1 MHz readout rate. To quantify the linearity of CCD response to optical signal, a region of interest (ROI, 30 pixel × 30 pixel) around maximum signal was chosen, and the averaged CCD counts in the ROI was plotted against exposure time. A linear least-squares regression analysis was chosen to fit the data. The deviation for each data point from the linear fit was calculated to characterize the CCD response linearity.

2.3 | Image background

To check background signal, open field (without filters) images with exposure time from 30 to 180 s were acquired at −90°, 0°, 90° and 180° projection with the same imaging parameters as common BLI acquisition, 10 × 10 binning, 4 × pre-amplifier, and 1 MHz readout rate. A ROI (60 binned pixel × 60 binned pixel, 61 mm × 61 mm) around image center was selected for analysis.

2.4 | Optical focusing

The position of focal plane was empirically set at 16 mm above the mouse bed to ensure that clear BLIs could be achieved, approximately at the mouse surface for a given imaging projection angle (see supporting material Section S1). To characterize the optical focusing

of MuriGlo, a rectangular self-illuminated light source (9 mm length × 2.8 mm width × 1.5 mm height, Trigalight, mb-microtec ag, Niederwangen, Switzerland) was placed on the center of the image at different heights above the mouse bed, and 1 × 1 binning images were acquired at open field, 590, 610, 630 and 650 nm. The profiles of light source placed at different heights were compared to characterize the focal plane position and the effect of optical focusing on 2D optical signals.

2.5 | Spatial resolution of 2D optical imaging

The spatial resolution of an imaging system is critical to assess the ability of the system to resolve fine structures. We used the contrast transfer function (CTF), a measurement of how contrast at a particular spatial resolution transfers from the object to the image, to determine the spatial resolution of 2D optical imaging on MuriGlo. A NBS 1963A negative resolution target (R2L2S1N, 2″ × 2″, Thorlabs, Inc., Newton, New Jersey, USA) was chosen for this test. We placed the resolution target on the center position within field of view at the focal plane of MuriGlo. To place the target precisely in the desired location, we used an in-house 3D printed support shown in Figure S2b, easily docked to the bed adaptor, where the target can be placed in the center. A 4″ × 5″ planar light source (Basic 95 CRI, Negative Supply LLC, Camarillo, California, USA) was placed below the bed to illuminate the resolution target through the rectangular opening (23 × 23 mm^2) of the support (Figure S2b). To increase uniformity of the illumination, a high-density polyethylene diffuser (HDPS-0250-E, Small Parts Inc., Logansport, IN) was placed on the light source. The default power supply of the light source was replaced with a multiple output DC power supply (MX180TP, Aim and Thurlby Thandar Instruments, Cambridgeshire, PE29 7DR, UK) at 7.2 V to adjust the light output for not saturating the CCD. To image different line pairs of the resolution target, we placed different line pairs on the opening. Images at 1 × 1 binning were acquired. CTF curves were generated by plotting the contrast of line pairs versus spatial frequency for both horizontal and vertical directions. We used Rayleigh criterion to define the spatial resolution of 2D optical imaging on MuriGlo based on the CTF curves. According to the Rayleigh criterion for two-point resolution, two equally bright points are just resolved when the center of one Airy disk falls on the first dark ring of the other Airy disk (see Figure S3). The contrast between the maximum intensity I_{max} and the minimum intensity I_{min} at the overlap (Figure S3) becomes 15%, calculated by $(I_{max} - I_{min})/(I_{max} + I_{min})$. Thus, we defined the spatial resolution of 2D optical imaging on MuriGlo when the line pairs are at 15% contrast level shown on the CTF curve.

2.6 | Image distortion

To detect potential image distortion, we designed a phantom with 3 mm-diameter circles in a grid pattern, with the circles placed regularly at 6.1 mm center-to-center spacing, as shown in Figure S2c. The phantom was printed by a stereolithography printer (Form 3B, Formlabs Inc., Somerville, Massachusetts, USA) at 0.1 mm dimensional accuracy. The phantom covering the imaging region of interest was designed to be easily placed on the bed adaptor. The photo image was acquired at 1 × 1 binning at 0° projection without filter and with LED on. The distance between the center of each circle and the center of the circle closest to the optical image center, called the reference circle, was measured from the optical image. The measured distance is defined as the pixel scale, which is 0.102 mm/pixel, times the number of pixels from a given circle center to the reference circle center. The deviation between the measured and actual distance, known from the circle grids, was used to quantify the image distortion of MuriGlo.

2.7 | Image uniformity

The non-uniformity of the optical image can be caused by lens vignette and the non-uniform response of CCD pixels. To examine the image uniformity of the optical system, we designed a phantom (Figure S2d), which allows rectangular self-illuminated light sources (9 mm length × 2.8 mm width × 1.5 mm height) placed in the grooves (9 and 11 mm for center to center spacing along the horizontal and vertical direction, respectively) on the phantom surface to form a 2D illumination array. This design allows us to measure the image uniformity of our optical system. To quantify the intensity variation of individual light source, we placed each source on the central groove of the phantom closest to the image center, and acquired images at 1 × 1 binning with open field and with 590, 610, 630 and 650 nm filters. The images of the 2D array with light source in place was also acquired at the same image acquisition setting. The intensity measured from the array image for each light source, within ROI of 10 pixel × 20 pixel at the center of the rectangular source, was normalized to its intensity measured on the central groove. Based upon this process, we can eliminate the intensity variation from individual light sources while quantifying image uniformity.

2.8 | Evaluation of the impact of the transparent plate applied for optical imaging

For our newly developed mouse bed, emitted bioluminescence can experience refraction, reflection, and attenuation through the transparent plate when the

object is imaged at 180° projection (Figure 1c). To assess if these factors could potentially affect BLI measurement, we imaged the mouse phantom inserted with a self-illumination light source (2 mm in diameter and 6 mm in length, Trigalight, mb-microtec ag, Niederwangen, Switzerland) for the scenarios with and without the transparent plate, respectively. The phantom images at 180° projection were acquired at 1 × 1 binning with 590, 610, 630, and 650 nm filters for both scenarios. For each scenario, five images were acquired for each wavelength, and the optical signal from these five images were averaged to reduce potential image noise. The averaged signal at each wavelength with the transparent plate was compared to that without the plate. We also studied the effect of the transparent plate on BLT reconstruction accuracy, with details described in Section 2.13.

2.9 | Dosimetric impact of the newly developed mouse bed

MuriPlan, a treatment planning system (TPS; version 2.2.2, Xstrahl Inc., Suwanee, Georgia, USA), is the standard platform utilized to design radiation plans for SARRP irradiation. For planning, MuriPlan only allows users to classify five materials, air, lung, fat, soft tissue, and bone, on SARRP CBCT images. Based on the image value, our mouse bed is commonly assigned as soft tissue. Our mouse bed consists of two kinds of material; one is RenShape SL 7820, an acrylonitrile butadiene styrene (ABS)-like material, used for the bed adaptor and the bed, and the other one is polycarbonate, used for the transparent plate. We assessed if there is any significant dosimetric difference when actual bed material, instead of the soft tissue, is used in dose calculation. We generated an artificial CBCT image consisting of two layers and assigned the bed material of interest to the first/bottom layer, and soft tissue to the second/top layer. We designed a radiation beam passing from the bottom to top layer with isocenter set at 9 mm above the bed material layer, and 5 Gy dose was prescribed at the isocenter. We generated the look-up tables of the x-ray mass attenuation coefficient for ABS and polycarbonate for dose calculation in MuriPlan.[23] The mass attenuation coefficient was calculated with $\mu/\rho = \sum_i w_i(\mu/\rho)_i$, where w_i is the faction by weight of the i^{th} atomic constituent of ABS ($C_8H_8 \cdot C_4H_6 \cdot C_3H_3N$) and polycarbonate ($C_{16}H_{16}O_4$), and $(\mu/\rho)_i$ is the mass attenuation coefficient for elemental media, obtained from the National Institute of Standards and technology database.[24] We then compared the dosimetric difference within the soft tissue/top layer for the cases of the first layer assigned as ABS/polycarbonate versus soft tissue. This planning setup allowed us to investigate if there is a significant dosimetric impact when the radiation beam passes through the bed and the soft tissue is assigned to the bed for dose calculation. For conservative measure and considering the worst scenario, such as oblique beam geometry, we simulated the first layer at 20 and 2.5 mm thickness when ABS and polycarbonate were assigned, respectively, despite the actual thickness for the bed and plate is at least two times less than the thickness in simulation. The dose calculation was performed for 3 × 3 mm^2, 5 × 5 mm^2, and 10 × 10 mm^2 collimation.

2.10 | Registration of 3D CBCT and 2D optical coordinates

Because the SARRP CBCT image defines the coordinates used for BLT reconstruction, we proposed a geometric calibration method modified from Cao et al.[25] to register the 3D CBCT coordinate and 2D optical imaging plane to map the 2D BLI acquired at a given projection angle onto the mesh surface generated from the CBCT image. Briefly, our geometric calibration approach includes two steps: (1) registering the 3D CBCT coordinate to 3D optical coordinates with rigid transformations, and (2) projecting the 3D optical coordinate to 2D optical coordinates at the CCD image plane that is the CCD sensor array. Once the 3D CBCT and 2D optical coordinates are registered, the 2D BLI acquired at any given projection angle can be mapped onto the mesh surface.

The orientations of 3D CBCT (O_s-$X_sY_sZ_s$), 3D optical (O-XYZ), and 2D optical (o-$\mu\nu$) coordinates are defined in Figure 2a. For the 3D optical coordinate, the Y axis is defined at the rotational axis of the three-mirror system and toward inside of the imaging chamber. The rotated 3D optical coordinate is defined as O-$X'Y'Z'$. For the rotation around the Y axis, the position where the three-mirror system is right above the mouse bed is labelled as 0°, the clockwise rotation is defined as the positive direction, and the range of rotation is defined from −180° to 180°. It is worthwhile to note that the mechanical definition of the mirror rotation is defined reversely, compared to the 3D optical coordinate rotation around the Y axis. The CCD image plane after multiple reflections through the mirror system is considered to be perpendicular to the Z axis or Z' axis after rotation (see Figure 2a). The 2D optical coordinate is located at the CCD image plane, and its axes, μ and ν, are parallel to the X and Y axes, respectively.

The registration between the 3D CBCT and 2D optical coordinates requires knowledge about the following 12 geometrical parameters.

1. X_{Ot}, Y_{Ot}, Z_{Ot}, translational shifts between the 3D CBCT and 3D optical coordinates.
2. δ_{Xs}, δ_{Ys}, δ_{Zs}, rotational shifts between the 3D CBCT and 3D optical coordinates.
3. L_{fd}, distance from the focal point, f, to the 2D optical image plane.

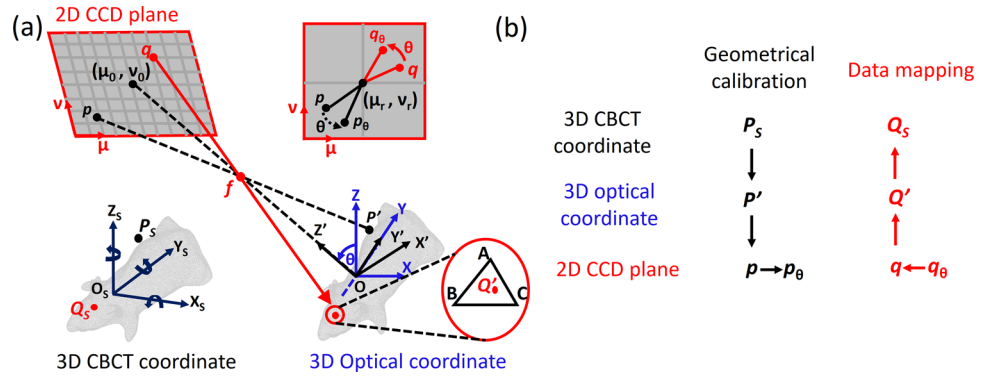

FIGURE 2 (a) and (b) show geometric relation among the 3D CBCT coordinate, 3D optical coordinate and 2D CCD plane, and workflow in geometrical calibration and data mapping procedure, respectively. For the geometrical calibration process, a fiducial marker P_S in the 3D CBCT coordinate was first linked to P' in 3D optical coordinate through rigid transformation. The P' in 3D optical coordinate was then projected to point p on 2D CCD plane based on ideal pinhole camera model, and rotated to p_θ by angle θ around (μ_r, ν_r) on 2D CCD plane when 3-mirror is rotated by θ as shown in the upper right subfigure in (a). For the data mapping, for a given q_θ on 2D CCD plane when 3-mirror rotated θ, a reverse procedure is used to calculate the corresponding position Q_S in 3D CBCT coordinate. 2D, two-dimensional; 3D, three-dimensional; CBCT, cone-beam computed tomography. CCD, charge-coupled device.

4. L_{fo}, distance from the focal point, f, to the 3D optical coordinate origin O.
5. μ_0, ν_0, center of the 2D optical image, intersection between the axis Z' in O-$X'Y'Z'$ with CCD image plane.
6. μ_r, ν_r, rotation center of 2D optical image; due to the three-mirror rotation with the static CCD camera, the 2D images were rotated accordingly during multi-projection imaging.

Rigid transformations, including translational and rotational shifts, were applied for registering the 3D CBCT coordinate to the 3D optical coordinate. For a given fiducial marker P_s in the imaging space, its position (P_{Xs}, P_{Ys}, P_{Zs}) in the 3D CBCT and (P_X, P_Y, P_Z) in the 3D optical coordinates is linked by

$$\begin{bmatrix} P_X \\ P_Y \\ P_Z \end{bmatrix} = R_{Xs}(\delta_{Xs}) \cdot R_{Ys}(\delta_{Ys}) \cdot R_{Zs}(\delta_{Zs}) \cdot \begin{bmatrix} P_{X_s} + X_{Ot} \\ P_{Y_s} + Y_{Ot} \\ P_{Z_s} + Z_{Ot} \end{bmatrix}, \quad (1)$$

where,

$$R_{Xs}(\delta_{Xs}) = \begin{bmatrix} 1 & 0 & 0 \\ 0 & \cos\delta_{Xs} & -\sin\delta_{Xs} \\ 0 & \sin\delta_{Xs} & \cos\delta_{Xs} \end{bmatrix}, \quad (2)$$

$$R_{Ys}(\delta_{Ys}) = \begin{bmatrix} \cos\delta_{Ys} & 0 & \sin\delta_{Ys} \\ 0 & 1 & 0 \\ -\sin\delta_{Ys} & 0 & \cos\delta_{Ys} \end{bmatrix}, \quad (3)$$

$$R_{Zs}(\delta_{Zs}) = \begin{bmatrix} \cos\delta_{Zs} & -\sin\delta_{Zs} & 0 \\ \sin\delta_{Zs} & \cos\delta_{Zs} & 0 \\ 0 & 0 & 1 \end{bmatrix}, \quad (4)$$

$R_{Xs}(\delta_{Xs})$, $R_{Ys}(\delta_{Ys})$ and $R_{Zs}(\delta_{Zs})$ are 3D rotation matrices with the rotation angles δ_{Xs}, δ_{Ys}, and δ_{Zs}, around X_s, Y_s and Z_s axes, respectively.

To project the 3D optical coordinate to the 2D optical coordinate at the CCD image plane, we modeled our CCD camera as an ideal pinhole camera. The projection geometry from the 3D optical coordinate after the mirror rotated at θ degree around Y axis to the 2D optical coordinate in pinhole camera modeling is shown in Figure 2a. No shift between Y and Y' axes was considered in this work. For the given point P_s, its corresponding position P in coordinate (O-XYZ) before and P' in coordinate (O-$X'Y'Z'$) after three-mirror rotation can be expressed as

$$\begin{cases} P'_{X'} = P_X \cdot \cos\theta + P_Z \cdot \sin\theta \\ P'_{Y'} = P_Y \\ P'_{Z'} = -P_X \cdot \sin\theta + P_Z \cdot \cos\theta \end{cases}. \quad (5)$$

With the pinhole camera modeling and Equation (5), the point (p_μ, p_ν) on the CCD image plane projected from the point P' can be expressed as

$$\begin{aligned} p_\mu &= \mu_0 + \frac{L_{fd} \cdot P'_{X'}}{F \cdot (L_{fo} - P'_{Z'})} \\ &= \mu_0 + \frac{L_{fd} \cdot (P_X \cdot \cos\theta + P_Z \cdot \sin\theta)}{F \cdot (L_{fo} + P_X \cdot \sin\theta - P_Z \cdot \cos\theta)}, \end{aligned} \quad (6)$$

$$\begin{aligned} p_v &= v_0 - \frac{L_{fd} \cdot P'_{Y'}}{F \cdot (L_{fo} - P'_{Z'})} \\ &= v_0 - \frac{L_{fd} \cdot P_Y}{F \cdot (L_{fo} + P_X \cdot \sin\theta - P_Z \cdot \cos\theta)}, \end{aligned} \quad (7)$$

where F is physical pixel size of the CCD sensor array, 13 μm/pixel for MuriGlo CCD.

The CCD camera is kept stationary while the three-mirror system is rotated during multi-projection image acquisition. In other words, from the view of the imaged object, the CCD plane is rotated in addition to the rotation around *Y* axis described above. Under this geometry, if the image is acquired after the three-mirror system is rotated by θ degree, the image projected at CCD plane will also be rotated by θ around the image rotation center (μ_r, ν_r). However, from the pinhole camera modeling, Equations (6)–(7), we do not consider this rotation. Therefore, the point p with coordinate (p_μ, p_ν) at the 2D optical coordinate, projected through the pinhole camera model, needs to be rotated by θ around (μ_r, ν_r) to be consistent with its position p_θ measured by CCD while three-mirror is rotated by θ. After rotation, p_θ, and its coordinate ($p_u(\theta)$, $p_v(\theta)$) can be expressed as

$$\begin{bmatrix} p_\mu(\theta) \\ p_v(\theta) \end{bmatrix} = \begin{bmatrix} \cos\theta & -\sin\theta \\ \sin\theta & \cos\theta \end{bmatrix} \cdot \begin{bmatrix} p_u - \mu_r \\ p_v - v_r \end{bmatrix} + \begin{bmatrix} \mu_r \\ v_r \end{bmatrix}. \quad (8)$$

From Equations (1–8), we can register any given point in the 3D CBCT volume to the 2D optical image at a given projection angle with the 12 geometrical parameters listed in 1–6. To retrieve these 12 parameters, we used the eight plastic ball bearings (BBs) on the mouse bed as fiducial markers (Figure 1c), which can be seen in photo images at -60°, -30°, 0°, 30°, and 60° projection and CBCT image. An optimization program with a constrained multivariable optimization function (fmincon; MATLAB R2019b, The MathWork Inc., Natick, Massachusetts, USA) was developed to retrieve the geometrical parameters by minimizing the deviation between the calculated and measured BB positions on the 2D CCD image plane. In this optimization routine, the BB positions in the multi-projection photo images are used as the measured positions, and the corresponding BB positions calculated based on Equations (1–8) with the optimized 12 parameters and the markers positions in 3D CBCT are used as the calculated positions. The deviation between calculated and measured BB positions could be minimized at < 0.3 mm, with average at 0.1 mm, by the optimization routine. To ensure accurate data mapping and relieve the requirement on mechanical reproducibility, the procedure of the geometric calibration is performed for each experiment, meaning every individual mouse or phantom imaging session. The procedure is fully automatic using the optimization routine without affecting experiment throughput.

2.11 | Data mapping for multi-projection BLIs

After the 3D CBCT and 2D optical coordinates are registered, we can utilize the geometrical parameters obtained from the Section 2.10 and reversely map the optical signal on the pixel of interest q_θ of a 2D BLI to the corresponding position Q_S on the mesh surface in 3D CBCT coordinate. The order of the mapping process is outlined in Figure 2b, $q_\theta \rightarrow q$ on 2D CCD plane $\rightarrow Q'$ in 3D optical coordinate $\rightarrow Q_S$ in 3D CBCT coordinate, and the detail is provided as follow.

The q_θ with coordinate ($q_u(\theta)$, $q_v(\theta)$) is the pixel of interest on the measured 2D BLI/CCD plane after the three-mirror is rotated by θ degree along the *Y*-axis. We first eliminate the mirror rotation for q_θ by considering the geometry, where there is no three-mirror in place, only single camera directly looking down the imaged object and it can rotate around the object to acquire projection image. We can perform the inverse of Equation (8);

$$\begin{bmatrix} q_\mu \\ q_v \end{bmatrix} = \begin{bmatrix} \cos\theta & \sin\theta \\ -\sin\theta & \cos\theta \end{bmatrix} \times \begin{bmatrix} q_\mu(\theta) - \mu_r \\ q_v(\theta) - v_r \end{bmatrix} + \begin{bmatrix} \mu_r \\ v_r \end{bmatrix}. \quad (9)$$

The q with coordinate (q_u, q_v) are the corresponding point for q_θ on the CCD plane as there is no mirror rotation.

The coordinate of q in *O-X'Y'Z'*, where the camera rotates θ degree, can be expressed by

$$\begin{cases} q_{X'} = -F \times (q_\mu - \mu_0) \\ q_{Y'} = F \times (q_v - v_0) \\ q_{Z'} = L_{fd} + L_{fo} \end{cases}. \quad (10)$$

The coordinate of focal point f can be written as (0, 0, L_{fo}) in the 3D optical coordinate *O-X'Y'Z'*. Thus, q and f can form a ray. We can use the Möller-Trumbore ray-triangle intersection algorithm[26] to locate the intersection Q' within a surface triangle on the imaged object mesh generated from the SARRP CBCT image. The barycentric coordinates is utilized in the Möller-Trumbore algorithm, which we can write the coordinate of the Q' as

$$Q' = aA + bB + cC = (1 - b - c)\,A + bB + cC. \quad (11)$$

A, B and C are the coordinates of the vertices for a triangle *ABC* in 3D optical coordinate *O-X'Y'Z'* (Figure 2a) and *a, b, c* are the barycentric coordinates of Q' for the triangle *ABC*. The intersection Q' can also be represented by a ray from q to Q' as

$$Q' = q + tD, \quad (12)$$

where t is the distance from Q' to q, and D is the normalized direction of the ray connecting q and f. By combining Equations (11) and (12), the unknowns t, b and c can be solved.

With the above-mentioned method, we can identify the barycentric coordinates, *a, b*, and *c* of the Q' for the triangle *ABC* in the 3D optical coordinate. Since the 3D CBCT and optical coordinates are rigidly registered

(Equation 1), we can apply the barycentric coordinates, *a, b*, and *c* to the corresponding triangle $A_sB_sC_s$ in the 3D CBCT coordinate with

$$Q_s = (1 - b - c)\ A_s + bB_s + cC_s, \tag{13}$$

and identify the position of Q_s to where we can map the pixel signal at q_θ. Here A_s, B_s and C_s are the coordinates of the vertices of triangle $A_sB_sC_s$ in 3D CBCT coordinate O_s-$X_sY_sZ_s$. For a given closed 3D mesh surface, there will be more than one intersection. The point Q_s we chose is the closest intersection to q.

To validate the accuracy of the data mapping method, 10 BBs were placed on a mouse phantom and imaged at −90°, 0°, 90° and 180° projections, commonly-used projection angles for the BLT, with the LEDs on. There were 8 BBs placed on the top surface of the phantom and 2 BBs placed on its bottom surface. The measured positions of the 10 BBs from these optical (LED) images were mapped to the mouse phantom surface in CBCT coordinate through the data mapping method, and compared to the BB positions measured in CBCT image. Because of the physical size of the BBs, the BB centers, shown in the CBCT image, were not on the phantom surface. We further calculated the corresponding positions of the BB centers on the phantom surface, so we can compare these positions with the BB positions mapped from the optical images. We first calculated the positions on 2D optical image plane using the centers of BBs in 3D CBCT coordinate and Equations (1–8) with the optimized geometrical parameters. We can then obtain the corresponding positions on the phantom surface using the calculated positions of the BB centers on 2D optical image plane along with Equations (9–13) through ray tracing. We can use these positions as the ground truth to validate the BB position mapped from the 2D optical image to the mesh surface in the CBCT coordinate.

We further provided the detail of our data selection protocol for BLT reconstruction. We first used 1 × 1 binning of the optical photo images for acquiring the position of the fiducial markers to ensure accurate registration between 3D CBCT and 2D optical coordinates (Section 2.10). For BLI acquisition, we utilized a larger binning size, 8 × 8 or 10 × 10 binning, to achieve sufficient signal to noise ratio (SNR) within reasonable imaging acquisition time. For the subsequent data mapping process, we used the position of the binned pixel center, representing the BLI signal of the pixel after binning, and mapped these points along with the pixel signal to the mesh surface generated from the 3D CBCT image. For the overlapped surface region mapped from two adjacent projection BLIs, if two mapped data are within the distance equal to the pixel scale after binning, for example, 1.02 mm for 10 × 10 binning, the mapped point with larger value will be chosen as the input data used for reconstruction. Moreover, we chose the mapped surface data points, with values larger than 10% of the maximum value among all the surface points and larger than an empirical threshold ∼1050 counts to remove the data close to background counts ∼950. The remaining data after the selection process become the input for subsequent reconstruction.

2.12 | Mathematical framework for BLT reconstruction

Because light transport in tissue is dominated by scattering, the Diffusion Approximation (DA) of the light transport equation was applied to model the light propagation in tissue. In continuous wave mode, the DA with the Robin-type boundary condition is expressed as

$$\begin{cases} -\nabla \cdot D(r)\,\nabla\Phi(r) + \mu_a(r)\,\Phi\ (r) = \ S(r)\,,\ r \in \Omega \\ \quad \Phi(\xi) + 2A\hat{n} \cdot D(\xi)\,\nabla\Phi\ (\xi) = \ 0,\ \xi \in \partial\Omega \end{cases}, \tag{14}$$

where $\Phi(r)$ is the photon fluence rate at location r in domain Ω, $D\ (r) = \ 1/(3(\mu_a + \mu_s'))$ is the diffusion coefficient, and μ_a and μ_s' are absorption and reduced scattering coefficients, respectively at a given wavelength λ. $S(r)$ is the bioluminescence source distribution. ξ represents points on the tissue boundary ($\partial\Omega$), and coefficient A can be derived from Fresnel's law, depending on the refractive index of tissue and air. $\hat{n}$ is the unit vector pointing outward, normal to the boundary $\partial\Omega$. Equation (14) can be further expressed in the form of linear function as

$$G_\lambda w_\lambda S\ = \ \Phi_\lambda, \tag{15}$$

where G_λ is the sensitivity matrix describing the changes of boundary/surface fluence rate Φ_λ related to source S for a given wavelength λ, and w_λ is the system-specific spectrum of the light source of interest. G_λ can be constructed from prior knowledge of the geometry and optical property of the subject.

In non-contact imaging geometry, one major challenging is accounting for the light propagation from animal surface to the optical detector (e.g., CCD). We have developed a SD method,[27] in which the SD of that data (the ratio of the surface images at adjacent wavelengths) is used, as bioluminescence at similar wavelengths encounters a near-identical system response. The system response can be expressed by rewriting $\Phi_\lambda = b_\lambda n$, where n is a measurement point specific angular dependent offset to account for the difference between actual surface fluence rate Φ_λ and BLI measurement b_λ, and n is assumed to be spectrally invariant. The Equation (15) becomes

$$G_\lambda w_\lambda S\ = b_\lambda\ n. \tag{16}$$

By applying logarithm to Equation (16) and considering the ratio of the data between two neighboring

wavelengths λ_i and λ_{i+1}, we can write the SD form of Equation (16) as

$$\left[\frac{\log b_{\lambda_i} n}{b_{\lambda_i} n} G_{\lambda_i} w_{\lambda_i} - \frac{\log b_{\lambda_{i+1}} n}{b_{\lambda_{i+1}} n} G_{\lambda_{i+1}} w_{\lambda_{i+1}}\right] S = \log \frac{b_{\lambda_i}}{b_{\lambda_{i+1}}}, \quad (17)$$

where the offset n in the right-hand side of the equation, caused by geometry shape of the imaged object and the free space light propagation from the object to camera, are cancelled out. The source distribution S in the SD form (Equation 17) can be iteratively solved by applying compressive sensing conjugate gradient (CSCG) optimization algorithm[27] with multi-spectral and multi-projection data. For this study, the ratios of the spectral data b_{590nm} / b_{610nm}, b_{610nm} / b_{630nm}, and b_{630nm} / b_{650nm} were chosen as the input for BLT reconstruction. The sensitivity matrix was generated by a modified version of NIRFAST software[28] under finite element framework. A tetrahedral mesh with an averaged edge length of approximately 1 mm was utilized for the finite element calculation as it is at the same order of mean free path of light scattering and the BLI pixel scale after 8 × 8 or 10 × 10 binning used in this study. The smaller mesh size may not improve reconstruction accuracy. The detail of mesh parameters can be found in supporting material Section. S2.

2.13 | BLT validation with mouse phantom

To access the target localization capability of the MuriGlo BLT, we inserted a small cylindrical self-illuminated light source (0.9 mm in diameter and 2 mm in length) into the mouse phantom and used it as the internal target for the study. We introduced a threshold between 0 and 1, based on the maximum value of BLT reconstructed power density (S, Equation 17), to define the target delineation. The positions where BLT reconstructed power density larger than the threshold of the maximum value were identified as part of the reconstructed target. Consequently, the position and volume of the reconstructed target could vary depending on the choice of threshold. We studied the MuriGlo BLT in target localization and volume delineation as function of threshold. We also extended the study for the cases with and without the transparent plate to investigate if the transparent plate could affect the BLT target localization.

The phantom underwent multi-projection at −90°, 0°, 90° and 180° and multi-spectral at 590, 610, 630 and 650 nm BLI acquisition. The BLIs were acquired with 30 s exposure time at 8 × 8 binning, 4× pre-amplifier gain, and 1 MHz readout rate with and without transparent plate. After acquiring BLIs, photo images at −60°, −30°, 0°, 30° and 60° projections were taken to retrieve the fiducial markers positions on the bed to obtain the geometric parameters (Section 2.10). After the optical imaging, the mouse phantom with the detachable mouse bed was docked to the bed adaptor pre-installed in SARRP for CBCT imaging. The CBCT image was used to (1) provide anatomical structure of the imaged object to generate tetrahedral mesh for the finite element method (FEM)-based BLT reconstruction and (2) define the 3D coordinate in SARRP for radiation planning and focal irradiation.

It is worth to note that the system-specific spectrum[15] of the small light source was measured on MuriGlo before phantom experiment. Because the half-life of the light source is 12.3 years, the source intensity was considered as time-invariant during spectrum measurement. The light source was placed on the MuriGlo mouse bed, and BLIs were acquired at 590, 610, 630, and 650 nm at 1 × 1 binning with 10 s exposure time. The light intensity measured at a given region of interest on 590, 610, 630, and 650 nm BLIs were normalized, and the normalized value 0.912, 1, 0.922, and 0.661 at 590, 610, 630 and 650 nm were used as the light source spectrum for the multi-spectral BLT reconstruction. The values of absorption coefficient μ_a 0.035, 0.010, 0.005 and 0.004 mm^{-1} and reduced scattering coefficient μ_s' 1.75, 1.66, 1.58 and 1.50 mm^{-1} for 590, 610, 630, and 650 nm, respectively, and refractive index 1.5, provided by Perkin Elmer, were used for the reconstruction.

2.14 | BLT validation with in vivo GBM model

All in vivo procedures were carried out in accordance with the institutional animal care and use committee at the University of Texas Southwestern Medical Center. To demonstrate the capability of MuriGlo in localizing in vivo GBM, we implanted 1.2 × 10^5 GL261-luc2 cells into the left striatum of C57BL/6J albino mice, 3 mm away from the surgical opening, and imaged the animal 2 weeks after surgery. For animal immobilization (Figure S4), the imaged mouse was anesthetized with 2% isoflurane in oxygen through the nose cone. We used rubber bands and taps on the bed to secure the limbs and tails. To prevent mouse ears blocking the surface signal during imaging acquisition at 90^0 and -90^0 projection, black tapes were used to press the ears down. The GBM-bearing mice underwent multi-projection at −90°, 0°, and 90° and multi-spectral at 610, 630, and 650 nm BLI acquisition at 10 × 10 binning, 4× pre-amplifier gain, and 1 MHz readout rate, followed by photo imaging at −60°, −30°, 0°, 30°, and 60° projections for geometric calibration. The bioluminescence signal at 590 nm was weak compared to other images, and therefore not used for the study. After the optical imaging, we transferred the mouse with the detachable bed to the bed adaptor pre-installed in SARRP for CBCT imaging.

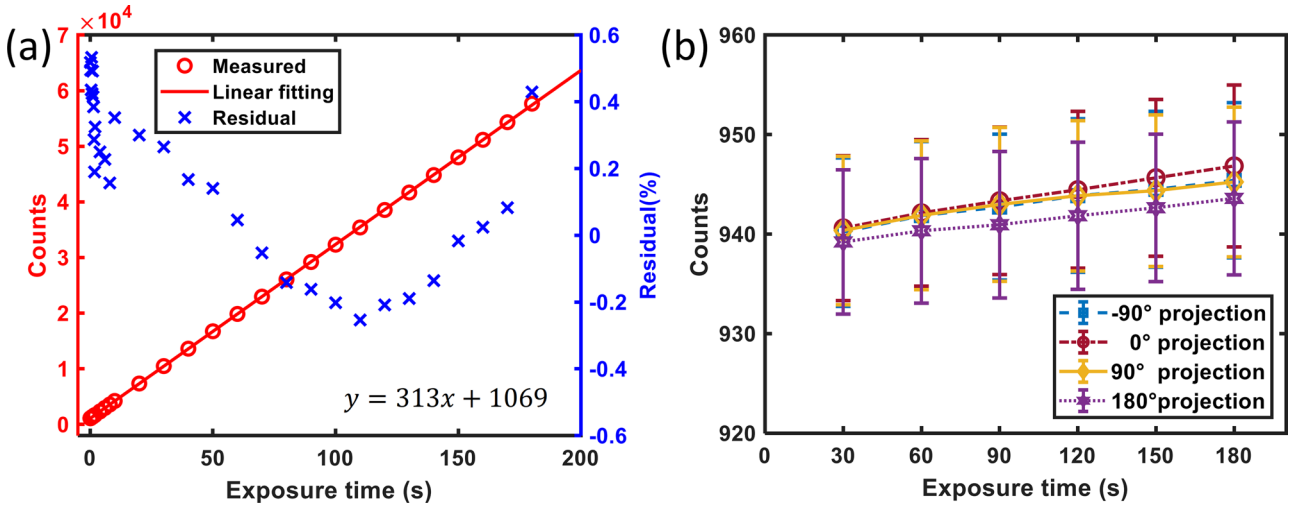

FIGURE 3 (a) shows the CCD counts increased linearly with exposure time. The residual shows the deviation of the measurement in percentage relative to the linear fitting. (b) shows the change of CCD counts of image background versus exposure time at −90°, 0°, 90° and 180° projection. CCD, charge-coupled device.

The system-specific GL261-luc2 cell spectrum was measured using the MuriGlo system as 1, 0.825, and 0.475 at 610, 630, and 650 nm, respectively. We used absorption coefficient μ_a 0.1610, 0.0820, and 0.0577 mm^{-1} and reduced scattering coefficient μ_s' 1.56, 1.51, and 1.46 mm^{-1} at 610, 630, and 650 nm, respectively, and refractive index 1.4 for BLT reconstruction. Based on our published study,[15] we used a threshold of 0.5 of maximum BLT reconstructed source power density to delineate the BLT reconstructed gross target volume (GTV_{BLT}). T_2-weighted fast spin echo sequence magnetic resonance imaging (MRI) (MRS 3017, 3T, MR Solutions Ltd. GU3 1LR, UK) was utilized to define the gross target volume (GTV) of GBM-bearing mice as the ground truth to validate the accuracy of BLT localization. The MRI and SARRP CBCT image of the mouse head were registered using 3D slicer (version 4.11.2; http://www.slicer.org). The registered GTV was compared with GTV_{BLT} to evaluate BLT localization accuracy.

3 | RESULTS

3.1 | Imaging characterization

Figure 3a shows that the CCD response is linear with the incident signal along with the CCD exposure time from 0.1 to 180 s. The overall residual deviation, the measured counts relative to the linear fit, is within 0.6%. For bioluminescence imaging, the in vivo signal strength is susceptible by various factors, for example, the choice of reporters, blood content within tissue, and number of bioluminescence cells. The 0.1 to 180 s range we investigated covers a practical exposure time used in daily operation.

Figure 3b shows the CCD counts of the image background at exposure time from 30 to 180 s. It shows that the largest image background is at 180 s at ~947.0 ± 8.1 counts for 10 × 10 binning, which indicates the minimal detectable signal level is about 972 counts with 3 standard deviations. The image background does not change significantly along with time for all the imaging projections, which suggests the light leakage to the imaging chamber is minimum.

Figure 4a shows representative profiles cross the center of light source for open field when the light source was placed at height of 1.5 and 14.5 mm above mouse bed. We noticed the size of the profile penumbra varies along with the height. As an imaged object was placed right at focal plane, one would expect to see a sharp image. To determine the focal plane position, we quantify the penumbra width; the smaller the penumbra width is, the sharper the image is. We used the convolution of Gaussian and rectangular function to fit the profiles. The penumbra, shadow region shown in Figure 4a, defined as the width between the 10% and 90% of the maximum intensity of the fitting curve, was used to quantify the broadening of the intensity profile. As shown in Figure 4b, the penumbra became wider when the light source was placed farther away from the focal plane. The focal plane position corresponding to minimum penumbra width is within the range of 13−18 mm above the bed for open and spectral images. We further investigated the effect of focusing on signal intensity (Figure 4c). The shoulder region of the profile shown in Figure 4a was chosen for data analysis, where the light intensity is sensitive to the change of the focal plane position. It shows a decrease in intensity of up to 17%, when the light source was placed off the focal plane. For the sake of visualization, we only plotted the standard deviation for the open field images, rendering large

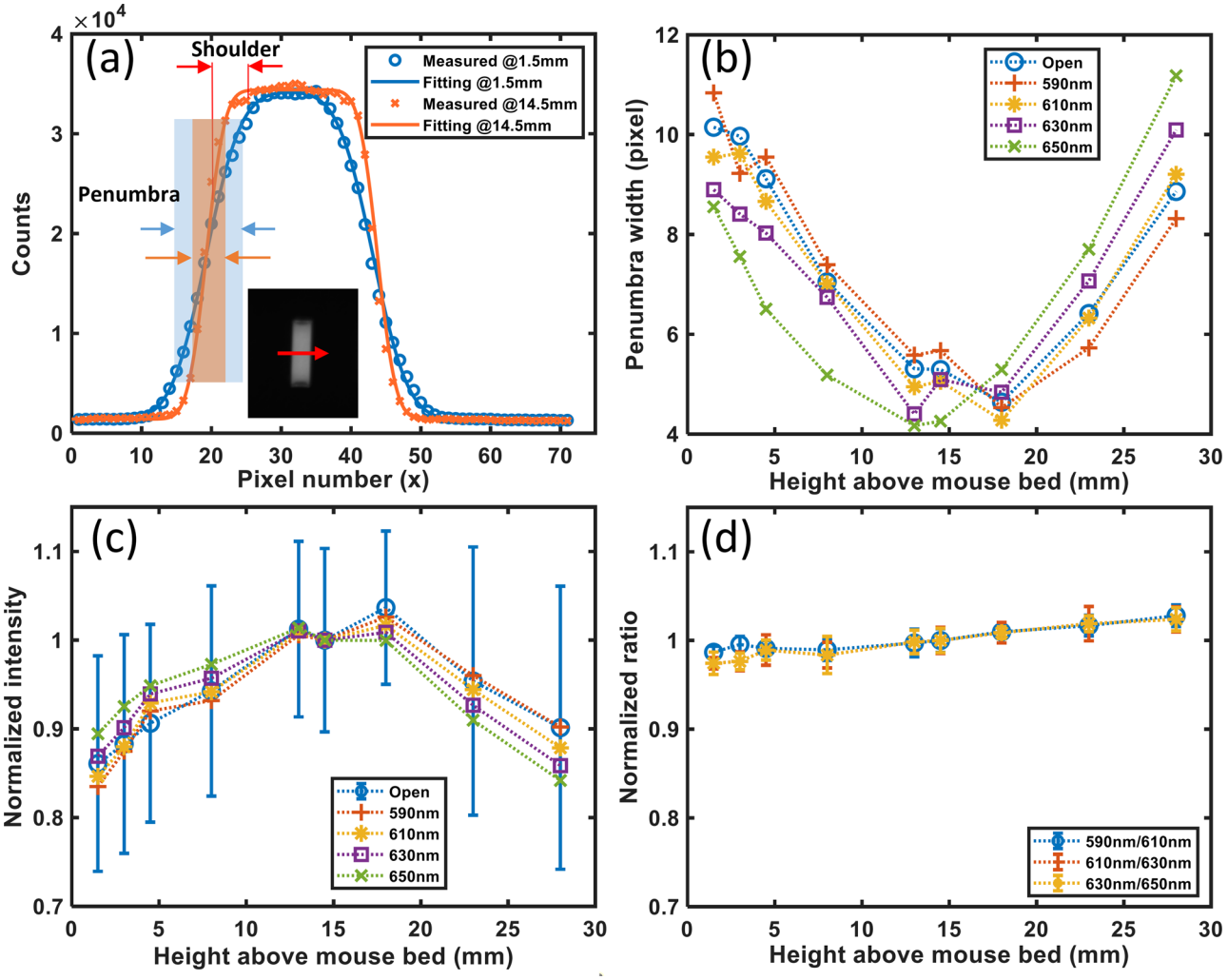

FIGURE 4 (a) shows the representative profile cross the center of light source (red arrow) at different height above the mouse bed measured at open field image. The penumbra width is defined between 10% –90% of maximum intensity of the fitting curve, shadow region. (b) shows the penumbra width of the profile, measured at different height above the bed for open field, 590, 610, 630 and 650 nm spectral images. (c) shows the averaged intensity within the shoulder region shown in (a), within pixel 20 to 25 of the profile, at different height above the bed for open field and spectral images. For the sake of visualization, only the standard deviation of the open field data points are shown. (d) shows the averaged ratio of the intensity and the standard deviation within the shoulder region at adjacent wavelength. The data in (c) and (d) was normalized to the value at 14.5 mm above the bed.

non-uniformity of the intensity within the shoulder region and the same phenomena was also seen in other wavelength cases (data not shown). Furthermore, the intensity variation is spectrally dependent because of chromatic aberration. Figure 4d further illustrates when the ratio of the intensity at adjacent wavelength is considered, the non-uniformity issue is largely improved, along with the reduction of variation, that is, standard deviation.

The inserted figure in Figure 5a shows a representative photo image of the NBS 1963A resolution target placed on the 3D-printed support (Figure S2b), acquired at 1×1 binning and 0° projection. The contrast of line pairs versus the spatial resolution (line pair/mm) was plotted in both X and Y directions (Figure 5a). With Rayleigh criterion (see Section 2.5), the resolution along X and Y directions are 2.27 lp/mm (0.22 mm) and 2.15 lp/mm (0.23 mm) by interpolating the line pairs at 15% contrast, respectively. Moreover, we measured the spatial resolution with filters at 590, 610, 630 and 650 nm, and the spatial resolution was superior to that of open field imaging (Figure S5a–b). We further measured the spatial resolution at different locations of the mouse bed region, by placing the resolution target at various locations (Figure S5c). Based on the Rayleigh criterion, we concluded MuriGlo can reach identifiable line pair number at 1.8 lp/mm or 0.28 mm of spatial resolution on the focal plane within entire mouse bed region for open field image (Figure S5d).

The inserted figure in Figure 5b shows the image of the distortion phantom acquired at 1 × 1 binning and 0° projection with white LED illumination and open field imaging. The centers of black circles are marked as

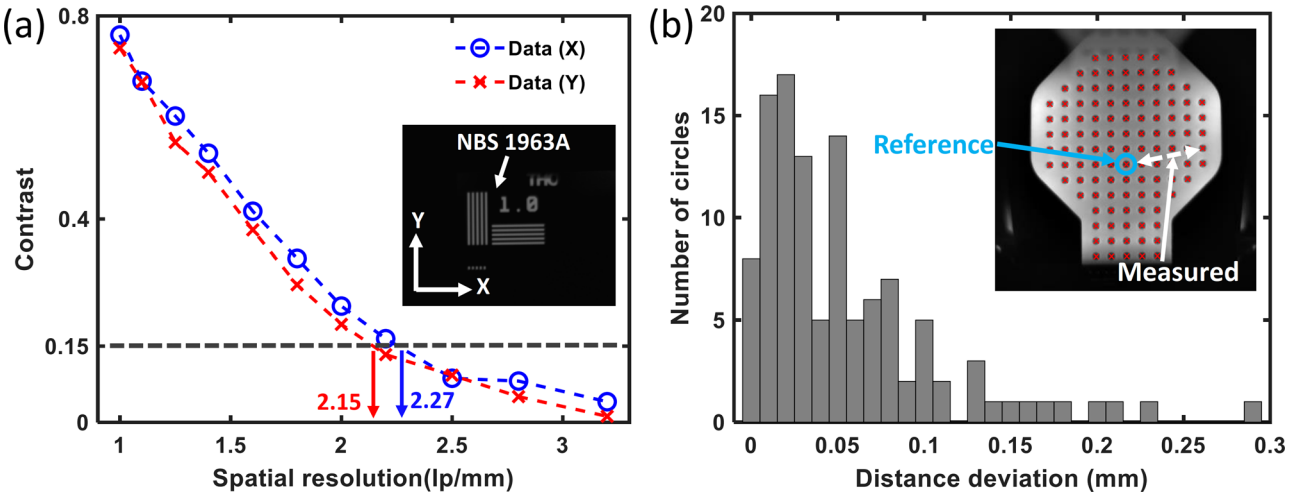

FIGURE 5 (a) shows contrast of line pairs versus spatial resolution at X and Y directions for an NBS 1963A negative resolution target placed on the 3D-printed support. The inserted figure shows a photo of 1.0 lp/mm line pair on the resolution target, placed on the 3D-printed support. (b) shows the histogram of the deviation between measured and actual distance from the center of circles on the distortion phantom to the reference center, shown in the right inserted figure, a photo of the distortion phantom. The centers of circles on the phantom were marked as red crosses. The measured distance (dash white arrow) was defined as the distance from a given center to the reference center (blue circle). 3D, three-dimensional.

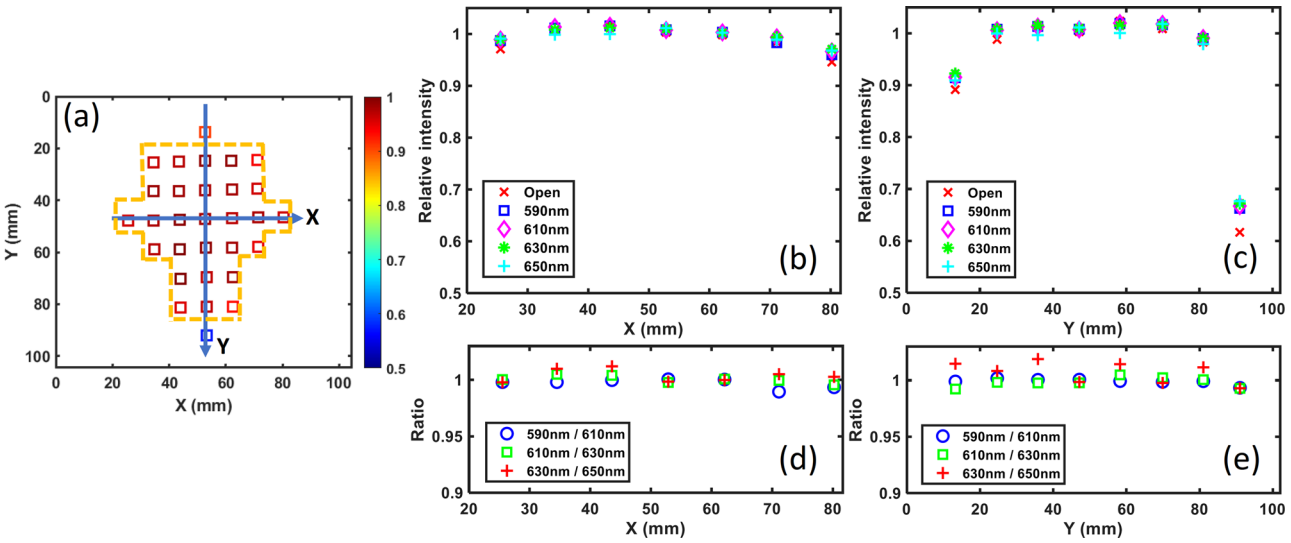

FIGURE 6 (a) shows the normalized intensity of the light sources at different locations placed on the uniformity phantom (Figure S2d) with open field imaging. The color at given location represents the image uniformity relative to the center position. (b–c) show the normalized light intensity of light source or image uniformity along the X and Y-arrow shown in (a) with open field and with filters at 590, 610, 630 and 650 nm, respectively. (d–e) show the corresponding ratio of the normalized light intensity at adjacent wavelength along the X and Y-arrow, respectively.

red crosses. The histogram of the deviation between the measured and actual distance from the center of all circles to that of the reference position is shown in Figure 5b. The average and maximum deviation is 0.05 ± 0.04 and 0.29 mm, respectively.

Figure 6a shows a representative plot of the image uniformity map with open field over the mouse bed region. The squares represent the center location of the light sources, and their colors indicate the image uniformity at their location relative to the center position. The yellow dashed box surrounds the region where the variation of uniformity is within 5%. We further plotted the normalized intensity along X and Y directions through the point closest to the image center (Figure 6b–c), which shows the uniformity is worsen close to both ends of mouse bed along the Y-axis. The obvious decrease of the uniformity could be up to 38% at the end of Y line (Figure 6c). This sharp decrease was due to the light cutoff by the front edge of the three-mirror system. However, after taking the ratio of the spectral images, the variation of the ratio data can be within 2% (Figure 6d–e). This means using

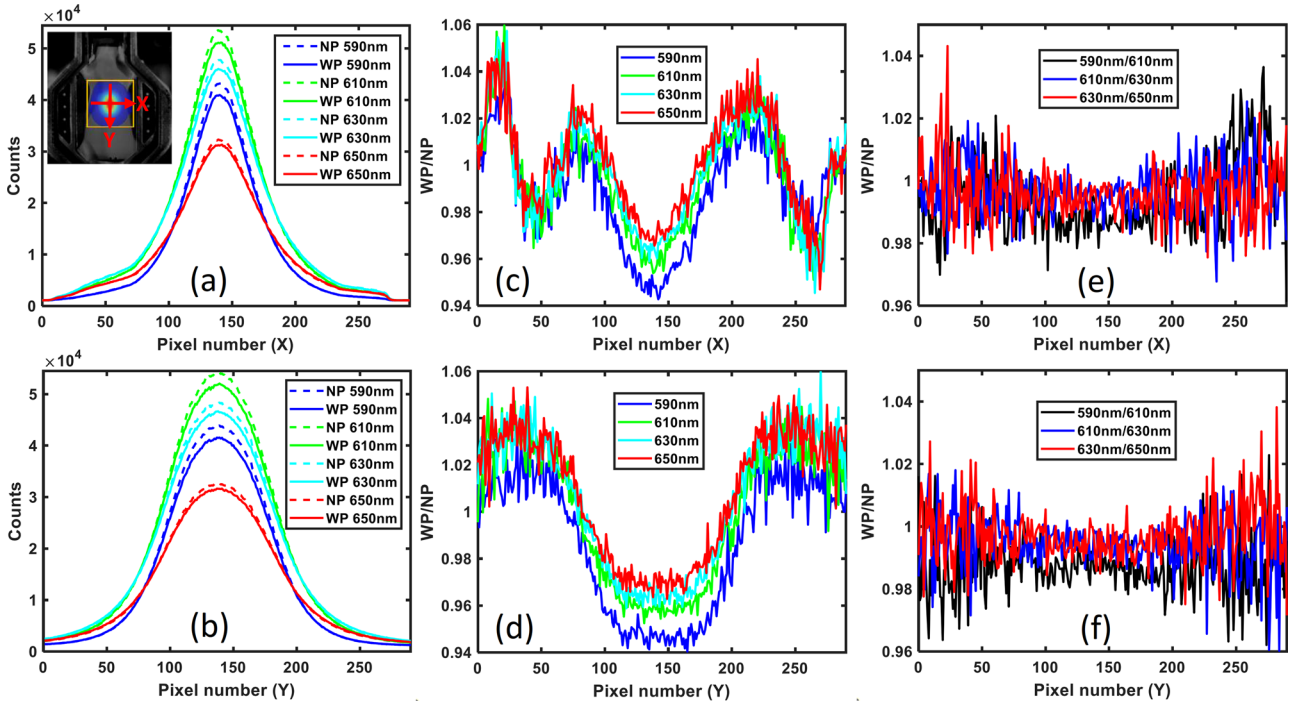

FIGURE 7 The inserted figure in (a) shows a representative bioluminescence image of phantom acquired at 180° projection and 610 nm with the transparent plate in place. (a–b) show the CCD counts profile along the X and Y-arrow, displayed in the inserted figure, at 180° projection and 590, 610, 630 and 650 nm for the cases with and without the plate, respectively. (c–d) show the ratio of CCD counts acquired with and without the plate along the X and Y-axis at 590, 610, 630 and 650 nm, respectively. (e–f) shows the corresponding ratio of the ratio images at adjacent wavelength along the X and Y-arrow with and without the plate, respectively. CCD, charge-coupled device. NP, no plate; WP, with plate.

SD data as the input for BLT reconstruction can minimize the image non-uniformity, which may affect the reconstruction accuracy.

3.2 | Assessment of the transparent plate applied for optical imaging and its impact on dosimetry

We assessed if the transparent plate on the bed (Figure 1c) could affect BLI measurement. As described in Section 2.8, we imaged the mouse phantom with a light source embedded. Figure 7a–b are the profiles of BLI acquired at 180° at all 4 wavelengths with and without the transparent plate along the X and Y axes, respectively, showing the light attenuation by the plate. To quantify the light attenuation observed in Figure 7a–b, we plotted the ratio of the profiles with and without the plate in Figure 7c–d. The plate caused <6% attenuation of light intensity for all spectral measurement. Since the SD data are used as the input for BLT reconstruction, we further calculated the ratio between the ratio of BLIs at adjacent wavelength with and without the plate. Figure 7e–f show that no significant difference is found if we employed the SD method for BLT reconstruction, while the plate is in place.

To quantify the dosimetric effect of the mouse bed material on dose calculation, we simulated the scenarios when the radiation beam passed through the bed at different thicknesses (1.25, 2.5, 5 and 20 mm) with three commonly used collimators (3 × 3, 5 × 5 and 10 × 10 mm^2). We compared the dose profiles vertically through the radiation isocenter for the cases of the mouse bed layer assigned as ABS/polycarbonate versus soft tissue. Even under the worst scenario, with the thickness at 20 mm for ABS material and 2.5 mm for polycarbonate, the difference in dose ratio is less than 0.5% (Figure 8). This result indicates that mouse bed segmented as soft tissue, the only option available in current version of SARRP treatment planning system, does not impact dosimetry significantly.

3.3 | Validation of data mapping for multi-projection BLIs

The procedure and validation of data registration between 2D BLI and 3D CBCT is demonstrated in Figure 9. Figure 9a shows eight fiducial markers used to retrieve the 12 geometrical parameters in the geometric calibration procedure (Section 2.10). To assess the accuracy of the calibration, we taped 10 BBs on the phantom; eight was on top surface of the phantom (Figure 9a), and two was on the bottom surface. The positions of these 10 BBs were directly measured from the 2D optical images taken at −90°, 0°, 90° and 180°

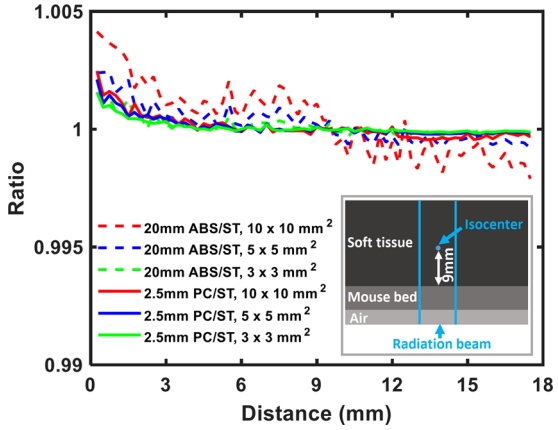

FIGURE 8 shows the ratio between the dose profiles of a radiation beam going through the isocenter with 20 mm-thick acrylonitrile butadiene styrene material or 2.5 mm-thick polycarbonate and that with "soft tissue" used as the mouse bed material in planning for 3×3, 5×5 and 10×10 mm^2 collimators. The inserted figure shows the layout of materials and radiation beam in the planning study. The isocenter was set 9 mm above mouse bed. A single dose of 5 Gy was prescribed at the isocenter. ABS, acrylonitrile butadiene styrene. PC, polycarbonate; ST, soft tissue.

projection, and were mapped to the phantom mesh surface generated from CBCT image with our data mapping method (Section 2.11). The mapped positions on the phantom surface from the measured BB positions on 2D optical image were compared to the reference position on the phantom surface calculated with the center of BBs in CBCT image (Figure 9b). The average and standard deviation between the mapped surface positions from measured and calculated positions of the BBs is 0.37 ± 0.01 mm ($n = 3$, three repeated experiments). The maximum deviation is 0.65 mm over all the BBs and the three test samples. This result indicates we can register multi-projection 2D optical images to 3D CBCT image at submillimeter accuracy.

3.4 | BLT validation with mouse phantom

To demonstrate the target localization accuracy of MuriGlo BLT and assess if the transparent plate would affect the optical reconstruction, the mouse phantom inserted with a small self-illumination light source was used for the study (Section 2.13). Figure 10a shows the 630 nm BLIs taken at −90°, 0°, 90° and 180° projections when the transparent plate is in place. Figure 10b is the corresponding BLIs mapped to the phantom mesh surface generated from the SARRP CBCT image. The light source seen in the CBCT image (white dot, Figure 10c–d, e–f) was taken as the ground truth, and the multi-projection and -spectral BLT-reconstructed light source with (Figure 10c–d) and without (Figure 10e–f) the SD method were overlapped with the CBCT image for comparison. It showed the SD method improves the BLT reconstruction results. Due to the non-symmetric BLT-reconstructed light distribution, the location of the center of mass (CoMs) of the BLT-reconstructed source volume can depend on the choice of threshold applied. Figure 10g shows that in general, we can reach ~ 1.5 mm BLT CoM localization accuracy regardless of the plate in place, in comparison with the source location shown in CBCT image. By further tuning the threshold, we can improve the localization accuracy to within 1 mm. We noticed that the transparent plate caused a systematic localization error, within 0.2 mm, compared to the cases without plate for all the threshold considered (Figure 10g). This deviation can be included into radiation margin design, when the transparent plate is used for the BLT-guided RT. It is understandable the BLT reconstructed source volume can vary depending on the choice of threshold. For this small light source, a high threshold such as 0.95 provides the best delineation of the light source. Overall, the relative difference between the BLT-reconstructed volumes with and without the plate is minimum, up to 8%. This 8% value is caused by the small volume difference between the cases with and without plate, when the BLT-reconstructed volume is applied with the threshold of 0.95.

3.5 | BLT validation with in vivo GBM model

Figure 11a shows the BLIs at 630 nm taken at −90°, 0° and 90° projections for a GBM-bearing mouse. The BLIs mapped to the mesh surface generated from the cropped mouse CBCT image is shown in Figure 11b, used as the input data for BLT reconstruction. The GTV_{BLT} based on the SD method was overlapped with the CBCT image (Figure 11c–e). The GTV contoured in the MRI (blue contour in Figure 11c–e) was taken as the ground truth and registered to the CBCT image to compare with GTV_{BLT}. The deviation of the CoM of GTV_{BLT} and the geometry center of GTV is at 0.69 mm. To account for the uncertainties of BLT localization and volume delineation, we added a uniform margin to GTV_{BLT} and formed a planning target volume (PTV_{BLT}) for radiation guidance. Without margin (0 mm expansion), the GTV was covered at 78% by GTV_{BLT}; with 0.5 mm margin expansion, the GTV can be covered at 97.9% by the PTV_{BLT} as shown in Figure 11c–e.

4 | DISCUSSION

Despite there is remarkable progress in the field of BLT-guided irradiation,[14–18] the development is still within academic laboratories. Our work is significant that we systematically characterized the performance of the commercial BLT system MuriGlo. We also advanced the

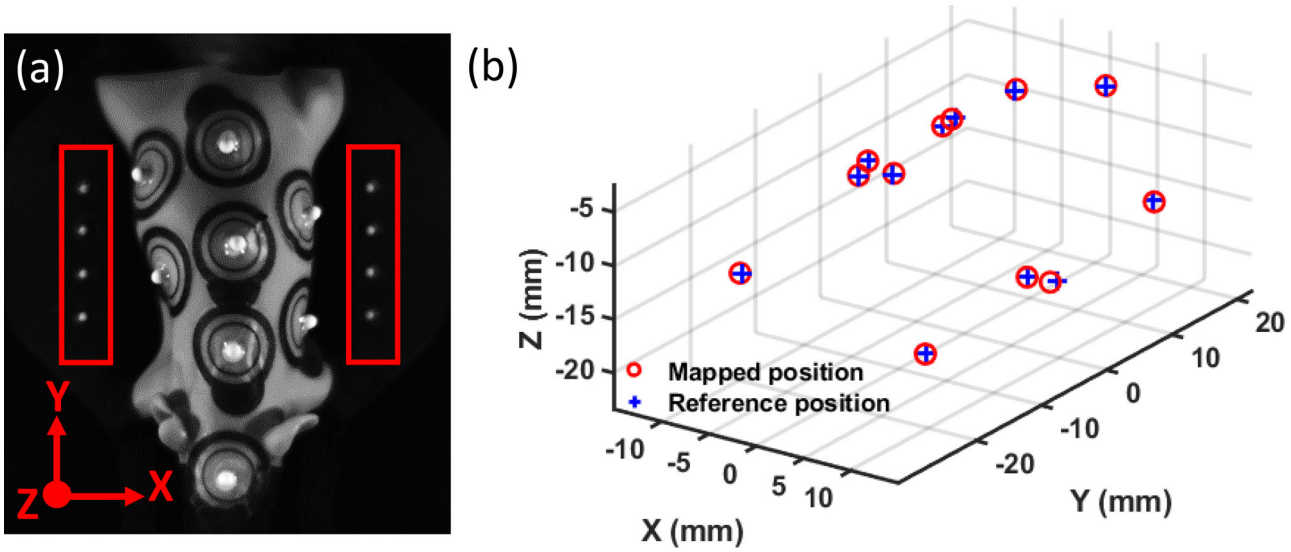

FIGURE 9 Validation of data registration between 2D optical images and 3D CBCT; (a) the BBs glued on the mouse bed, within red rectangles, were used as the fiducial markers to retrieve the geometric parameters for data mapping, and the BBs taped on the mouse phantom were used to assess the accuracy of the mapping. The axis of optical image coordinate related with the axis of the 3D CBCT coordinate is labelled. (b) Validation of data mapping from 2D bioluminescence images to 3D CBCT image; red circles represent the mapped positions on the mouse phantom surface in 3D CBCT coordinate, directly mapped from the measured BB positions on 2D optical images, and the blue crosses represent the reference positions on the mouse phantom surface, calculated from the centers of BBs in CBCT image. 2D, two-dimensional; 3D, three-dimensional; BB, ball bearing; CBCT, cone-beam computed tomography.

existing configuration in both hardware and algorithm aspects, specifically, developing the detachable mouse bed, the SD approach and the advanced 2D BLI and 3D CBCT image registration.

As compared to the commonly used single projection optical imaging system,[29,30] MuriGlo is equipped with a rotary three-mirror design to provide 360° multi-projection images. It allows MuriGlo to maximize the collected surface signal used as the input for BLT reconstruction while animal is placed in a nature comfort position, such as prone setup. The natural position eases the requirement for animal immobilization and transport between MuriGlo and SARRP, which could maintain experiment reproducibility. Because the actual tumor location is usually unknown, single projection imaging has limitation of capturing all surface signal for BLT reconstruction. In contrast, the multi-projection imaging approach provides users the options of where to image and how many projections to use for reconstruction. Especially for abdominal site, such as pancreatic tumor, single projection imaging could not always capture all the surface signal as the tumor could move to different location at a given imaging day.[31] The multi-projection imaging approach would resolve this concern. Furthermore, as compared to the system with rotating camera,[32] the rotation of the mirror allows for compact system and mechanical configuration. Moreover, we utilized the standalone design (Figure 1). Optical system is often used for longitudinal studies or tumor monitoring when irradiation guidance and 3D imaging are not needed. Small animal irradiators, for example, SARRP in our institution, are commonly used as core equipment shared by many laboratories, so the availability and throughput are important for such frequently used equipment. In addition, the mechanical design of on-boarding optical system can be irradiator-specific,[12] making it difficult retrospectively fitting the optical system to different irradiator models. Given these considerations, we utilized the standalone setting while ensuring stable animal transportation between the optical and radiation systems, enabling optimal utilization of both systems. The design of the mouse bed is innovative as it enables a convenient and fast workflow for users; when the BLI is finished, one can unplug the detachable bed from the bad adaptor and quickly move the bed to another adaptor in the irradiator (Figure 1a). Regarding the potential positioning error caused by animal transportation, as shown in a previous study,[33] the positioning error can be maintained within 0.2 mm as long as the animals are anesthetized with effective immobilization during transportation (Figure S4) and the BLT system is in close proximity (<5 m) to the irradiator. Most importantly, when we mapped the 2D BLIs to the surface of 3D mesh generated from the CBCT image, this positioning error, if present, either rigid or non-rigid error, will be propagated to the data mapping, and finally to the BLT reconstruction, which can be accounted for in radiation margin design.[15] In terms of dosimetric concern, the materials of the bed only gave rise to <0.5% dosimetric difference when the bed was segmented as soft tissue (Figure 8), which largely simplifies treatment planning procedure without specific material assigned.

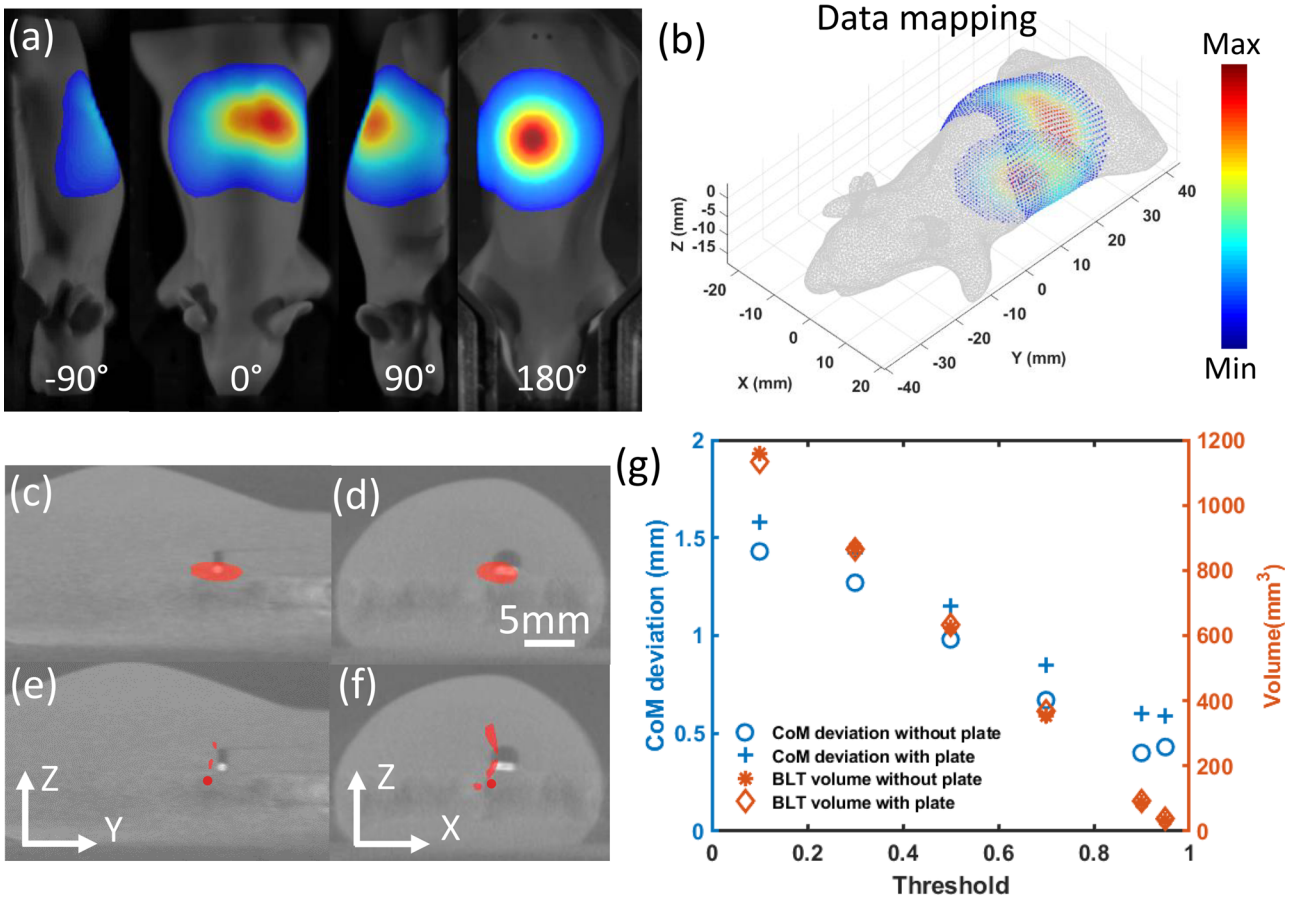

FIGURE 10 (a) shows 630 nm bioluminescence images of the mouse phantom at −90°, 0°, 90° and 180° projections where the transparent plate is in place. (b) is the corresponding bioluminescence images mapped onto the mesh surface of the phantom. Data >10% of maximum mapped data value is displayed. (c-d and e-f) are the BLT-reconstructed light source with and without spectral derivative method applied, delineated by a threshold of 0.95 (> 0.95 of maximum BLT reconstructed value) and 0.5, respectively. The white dot in the images is the actual light source. (g) shows the deviation between the center of mass of BLT- and the center of CBCT-reconstructed light source and the volume of BLT-reconstructed light source versus threshold for the cases with and without the transparent plate. BLT, bioluminescence tomography; CBCT, cone-beam computed tomography.

From Figure 3a, the CCD response of the MuriGlo system is linear within the range of imaging acquisition time commonly used for BLI acquisition, which ensures the system to be used for longitudinally signal monitoring. Regarding the image background (Figure 3b), we observed a slight increase in the background signal of approximate 6 counts within an exposure time range of 30 to 180 s. It renders that the background signal is mainly originated from readout noise, because dark current and light leakage would increase with exposure time, and they are minimum in the MuriGlo setting.

The position of the camera focal plane was set to ensure that clear BLIs were achieved approximately at the mouse surface for a given imaging projection. By considering mouse size and depth of field, we empirically set the MuriGlo focal plane at ~16 mm above the bed, to cover the mouse surface for 360° imaging (Figure S6a–d). As part of our quality assurance practice, we also developed a wedge phantom to allow us quickly check the focusing position (Figures S2a and S6e-f), as well as a focus lock to maintain consistent focusing setting (Figure 1b).

The spatial resolution of 2D optical imaging on MuriGlo is 0.28 mm on the focal plane within entire mouse bed (Figure S5d). Despite the resolution is constrained by CCD pixel size, large pixel binning is often used to improve the signal-to-noise ratio for BLI and due to the nature of tissue scattering at the order of 1 mm within the bioluminescence wavelength range, the requirement of image resolution for the surface BLI is less stringent. We recognized it is challenging to quantify the spatial resolution of the 3D BLT as it depends not only on the reconstruction algorithm, but also on the depth of the target located and tissue type. Because the light scattering in tissue is at the order of 1 mm, the spatial resolution of the BLT to distinguish two targets will be more than 1 mm. From our previous work,[34] as the depth of target increases, the larger separation is needed for BLT to resolve two targets, meaning worse spatial resolution in deeper depth due to strong scattering effect. With a conjugate gradient algorithm,[34] the

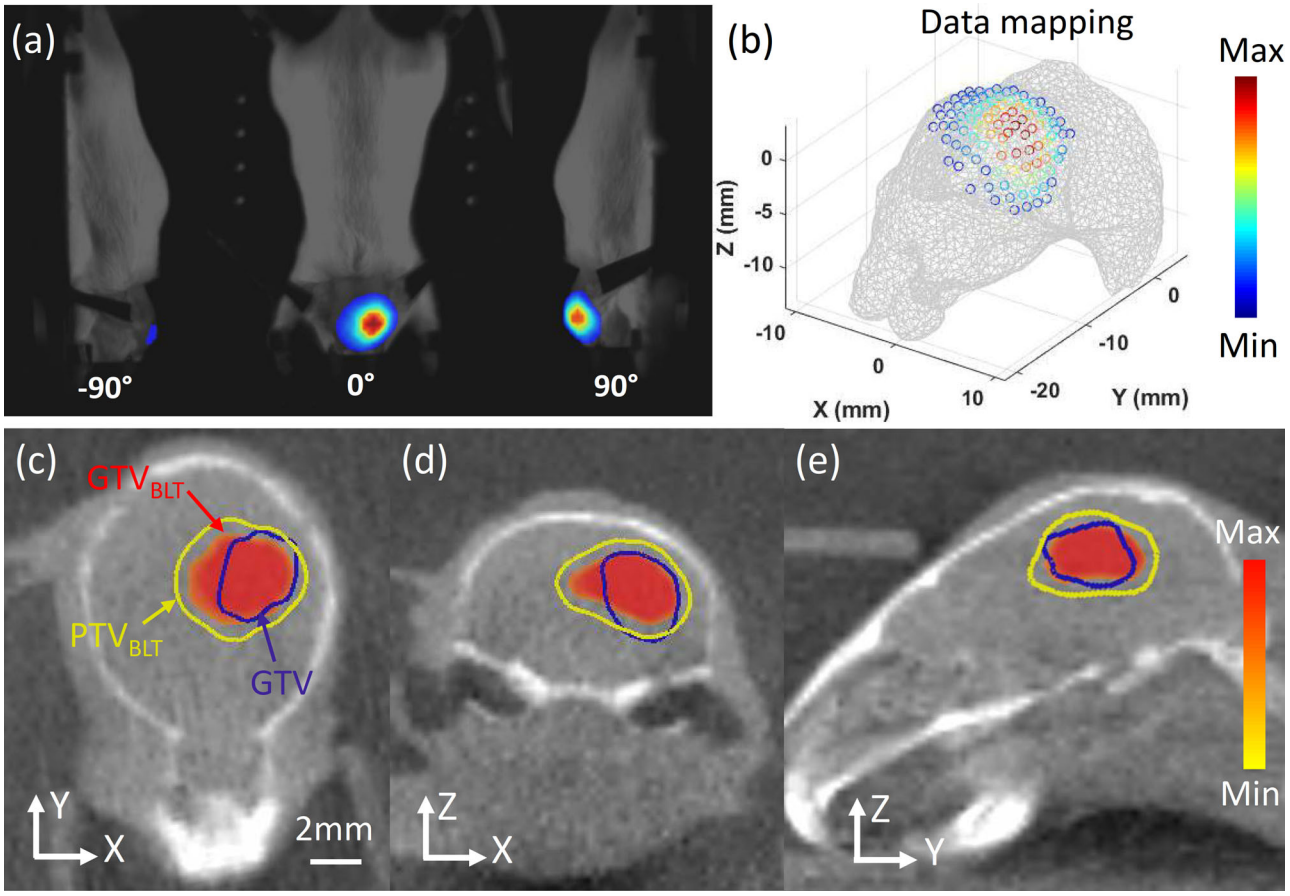

FIGURE 11 (a) shows 630 nm bioluminescence images of a 2nd week glioblastoma-bearing mouse acquired at −90°, 0°, and 90° projections. (b) is the corresponding bioluminescence images mapped onto the mesh surface of the mouse head. Data > 10% of maximum mapped data value is displayed. (c–e) are three views of CBCT image overlapped with gross target volume (GTV, blue contour), BLT reconstructed gross target volume (GTV_{BLT}, heat map) and planning target volume (PTV_{BLT}, yellow contour, 0.5 mm margin). BLT, bioluminescence tomography; CBCT, cone-beam computed tomography; GTV, gross target volume; PTV, planning target volume.

BLT could distinguish two sources separated at 3 mm at the depth of 5 mm in mouse abdomen. Establishing a universal method to quantify the spatial resolution of 3D BLT in vivo is a challenging task. However, for the purpose of radiation guidance, if two tumors are in proximity, these tumors are likely considered as single target for irradiation given the reason of experiment throughput and simplicity.

Since there was no obvious image distortion observed (Figure 5b), no image distortion correction was applied. We further quantified the image uniformity; for the most of the bed region, the uniformity is within 5% except in the area close to both ends of the bed along the Y-axis (Figure 6a). This result is informative when one wants to use BLI only for qualitative signal monitoring, to avoid the data originated from the non-uniformity area as it could mislead experiment interpretation.

One important innovation of this work is the use of SD data or ratio images, instead of individual spectral image, as the input for tomographic reconstruction. The measured intensity of BLIs depend on the position and viewpoint of the animal to the optical detector due to free-space light propagation. This can lead to inconsistent surface signal, even one images the same surface area and the corresponding signal is from the same internal bioluminescent source. We had proposed the theory that the SD approach can eliminate the geometric dependence of the free-spacing light detection.[27] In this work, we further examined its ability in alleviating the image intensity variation due to focusing (Figure 4a,c vs. Figure 4d). Because of the chromatic aberration, as illustrated in Figure 4b,c, we showed the focusing position is function of wavelengths and it can also affect the measured intensity away from the focal plane. By considering the ratio images, we can effectively eliminate the concern of out of focusing when multi-spectral imaging is used (Figure 4c vs. Figure 4d). The SD approach can also be applied to resolve the image non-uniformity (Figure 6b,c vs. Figure 6d-e), and light attenuation (Figure 7a-b,c-d vs. Figure 7e-f) due to optics and the transparent plate, respectively, which lead to the input data (ratio images) free of these variations for the optical reconstruction.

Since CBCT images provide the anatomy coordinates of the imaged animal, used for radiation delivery and optical reconstruction, it is important to ensure 2D BLI accurately mapped to the 3D CBCT image. After the mapping, the BLT reconstructed source can be defined in the CBCT coordinate system and ready for irradiation. From our previous mapping method,[18] for a given position on the mesh surface generated from an animal CBCT, we can find the corresponding location on 2D optical coordinates, and map this bioluminescence intensity back to the 3D mesh surface. However, depending on how the mesh was configured, the number of data mapped to the 3D mesh surface can vary. To eliminate this mesh dependence and facilitate the result comparison among different mice or imaging sessions, we developed a new mapping method (Sections 2.10–2.11) which allows us directly to map a pixel in 2D BLI to the mesh surface and used the pixel value as the input for BLT reconstruction. The new method allows multiple projection BLIs mapped to CBCT coordinates at <0.7 mm accuracy, with the average error < 0.4mm (Figure 9b).

With all the above-mentioned methodologies, we showed the target localization capability of the MuriGlo system with phantom and in vivo orthotopic GBM model. The SD method largely reduced the imaging uncertainties and thus improved the BLT reconstruction accuracy, compared to the traditional reconstruction approach (Figure 10c-d vs. Figures 10e-f). It is a known challenge to delineate targets or tumors based on optical tomographic imaging due to the nature of diffusive light in tissue medium. An empirical threshold of maximum reconstructed value is commonly used to define target distribution in optical tomography studies.[35–37] Figure 10g shows that the threshold used could affect the target localization accuracy and volume delineation. Due to the small cylindrical light source (0.9 mm in diameter and 2 mm in length) used in this study, we found the increase of the threshold leading to higher localization accuracy; with the threshold ≥ 0.5, we can reach < 1 mm image-guided accuracy. With the transparent plate in place, there is a small 0.2 mm localization uncertainty caused by the plate but not affecting the volume delineation. Nevertheless, our group has proposed[15] adding a margin to consider the uncertainties in target positioning and delineation for BLT-guided irradiation, as well as other systematic uncertainties, for example, radiation delivery error.

With an optimized threshold 0.5 obtained from our previous study using a prototype system,[15] we could reach in vivo BLT GBM localization < 1 mm (Figure 11c–e) with MuriGlo. We further compared the BLT localization (0.61 ± 0.40 mm, $n = 4$ vs. 0.62 ± 0.16 mm, $n = 10$) and GTV coverage by PTV_{BLT} with 0.5 mm margin (94.5 ± 4.8%, $n = 4$ vs. 97.9 ± 3.5%, $n = 10$) between MuriGlo and our prototype system[15]; there is no significant difference ($p > 0.05$). It indicates that the commercial platform MuriGlo can achieve the similar BLT localization accuracy of our prototype system.[15] Despite the in vivo BLT localization results with homogeneous optical property applied is encouraging and reproducible, the region with relative heterogeneous optical property could potentially affect BLT reconstruction accuracy. Our group is advancing the published algorithm,[38] which will allow the reconstruction of spatially heterogeneous optical properties while the reconstructed optical properties can be iteratively feedback to the BLT algorithm to improve localization accuracy. We recognize the animal validation shown in this work is a fraction of in vivo BLT-guided radiation research. To provide a comprehensive methodology and planning strategies regarding how to apply the MuriGlo for radiation guidance, we are preparing a follow-up manuscript for publication.

In summary, the integration of the elaborate hardware design, the advanced reconstruction algorithm, and the strategy of using BLT delineated volume and radiation margin allows MuriGlo to guide clinically relevant radiation therapy precisely on small animal irradiators.[15,18]

5 | CONCLUSION

We developed a systematic method to characterize a commercial BLT system for preclinical radiation guidance. This work is the first comprehensive study of MuriGlo performance in 2D optical imaging and 3D BLT target localization. The knowledge and methods developed in this study provide a guidance for MuriGlo users across different institutes to implement accurate image-guided radiation research, which will ultimately improve study reproducibility.

ACKNOWLEDGMENTS

This work was supported by the grants from National Cancer Institute, National Institutes of Health of USA (R21CA223403, R37CA230341, and R01CA240811) and Cancer Prevention and Research Institute of Texas RR200042, and RP180770.

CONFLICT OF INTEREST STATEMENT

The research group of Dr. Ken Kang-Hsin Wang and Xstrahl are supported by NIH academic-industrial partnership R37CA230341 in the development of BLT-guided system for pre-clinical radiation research.

REFERENCES

1. de Jong M, Maina T. Of mice and humans: are they the same?–implications in cancer translational research. *J Nucl Med*. 2010;51(4):501-504. doi:10.2967/jnumed.109.065706
2. Brown KH, Ghita M, Dubois LJ, et al. A scoping review of small animal image-guided radiotherapy research: advances, impact

and future opportunities in translational radiobiology. *Clin Transl Radiat Oncol*. 2022;34:112-119. doi:10.1016/j.ctro.2022.04.004
3. Graves EE, Zhou H, Chatterjee R, et al. Design and evaluation of a variable aperture collimator for conformal radiotherapy of small animals using a microCT scanner. *Med Phys*. 2007;34(11):4359-4367. doi:10.1118/1.2789498
4. Wong J, Armour E, Kazanzides P, et al. High-resolution, small animal radiation research platform with x-ray tomographic guidance capabilities. *Int J Radiat Oncol Biol Phys*. 2008;71(5):1591-1599. doi:10.1016/j.ijrobp.2008.04.025
5. Clarkson R, Lindsay PE, Ansell S, et al. Characterization of image quality and image-guidance performance of a preclinical microirradiator. *Med Phys*. 2011;38(2):845-856. doi:10.1118/1.3533947
6. Pidikiti R, Stojadinovic S, Speiser M, et al. Dosimetric characterization of an image-guided stereotactic small animal irradiator. *Phys Med Biol*. 2011;56(8):2585-2599. doi:10.1088/0031-9155/56/8/016
7. Verhaegen F, Granton P, Tryggestad E. Small animal radiotherapy research platforms. *Phys Med Biol*. 2011;56(12):R55-83. doi:10.1088/0031-9155/56/12/R01
8. Sha H, Udayakumar TS, Johnson PB, Dogan N, Pollack A, Yang Y. An image guided small animal stereotactic radiotherapy system. *Oncotarget*. 2016;7(14):18825-18836. doi:10.18632/oncotarget.7939
9. Sadikot RT, Blackwell TSB. Bioluminescence imaging. *Proc Am Thorac Soc*. 2005;2(6):511-532. doi:10.1513/pats.200507-067DS
10. Zinn KR, Chaudhuri TR, Szafran AA, et al. Noninvasive bioluminescence imaging in small animals. *ILAR J*. 2008;49(1):103-115. doi:10.1093/ilar.49.1.103
11. Mezzanotte L, van 't Root M, Karatas H, Goun EA, Lowik CWGM. In vivo molecular bioluminescence imaging: new tools and applications. *Trends Biotechnol*. 2017;35(7):640-652. doi:10.1016/j.tibtech.2017.03.012
12. Zhang B, Wang KK, Yu J, et al. Bioluminescence tomography-guided radiation therapy for preclinical research. *Int J Radiat Oncol Biol Phys*. 2016;94(5):1144-1153. doi:10.1016/j.ijrobp.2015.11.039
13. Klose AD, Paragas N. Automated quantification of bioluminescence images. *Nat Commun*. 2018;9(1):4262. doi:10.1038/s41467-018-06288-w
14. Shi J, Udayakumar TS, Wang Z, Dogan N, Pollack A, Yang Y. Optical molecular imaging-guided radiation therapy part 1: integrated x-ray and bioluminescence tomography. *Med Phys*. 2017;44(9):4786-4794. doi:10.1002/mp.12415
15. Xu X, Deng Z, Dehghani H, et al. Quantitative bioluminescence tomography-guided conformal irradiation for preclinical radiation research. *Int J Radiat Oncol Biol Phys*. 2021;111(5):1310-1321. doi:10.1016/j.ijrobp.2021.08.010
16. Deng Z, Xu X, Garzon-Muvdi T, et al. In vivo bioluminescence tomography center of mass-guided conformal irradiation. *Int J Radiat Oncol Biol Phys*. 2020(3):612-620. doi:10.1016/j.ijrobp.2019.11.003
17. Shi J, Udayakumar TS, Xu K, Dogan N, Pollack A, Yang Y. Bioluminescence tomography guided small-animal radiation therapy and tumor response assessment. *Int J Radiat Oncol Biol Phys*. 2018;102(4):848-857. doi:10.1016/j.ijrobp.2018.01.068
18. Deng Z, Xu X, Iordachita I, et al. Mobile bioluminescence tomography-guided system for pre-clinical radiotherapy research. *Biomed Opt Express*. 2022;13(9):4970-4989. doi:10.1364/BOE.460737
19. Chaudhari AJ, Darvas F, Bading JR, et al. Hyperspectral and multispectral bioluminescence optical tomography for small animal imaging. *Phys Med Biol*. 2005;50(23):5421-5441. doi:10.1088/0031-9155/50/23/001
20. Dehghani H, Davis SC, Jiang S, Pogue BW, Paulsen KD, Patterson MS. Spectrally resolved bioluminescence optical tomography. *Opt Lett*. 2006;31(3):365-367. doi:10.1364/ol.31.000365
21. Rapic S, Samuel T, Lindsay PE, Ansell S, Weersink RA, DaCosta RS. Assessing the accuracy of bioluminescence image-guided stereotactic body radiation therapy of orthotopic pancreatic tumors using a small animal irradiator. *Radiat Res*. 2022;197(6):626-637. doi:10.1667/RADE-21-00161.1
22. Rezaeifar B, Wolfs CJA, Lieuwes NG, et al. A deep learning and Monte Carlo based framework for bioluminescence imaging center of mass-guided glioblastoma targeting. *Phys Med Biol*. 2022;67(14):144003. doi:10.1088/1361-6560/ac79f8
23. Cho N, Tsiamas P, Velarde E, et al. Validation of GPU-accelerated superposition-convolution dose computations for the small animal radiation research platform. *Med Phys*. 2018;45(5):2252-2265. doi:10.1002/mp.12862
24. NIST standard reference database 126. doi:10.18434/T4D01F
25. Cao LJ, Breithaupt M, Peter J. Geometrical co-calibration of a tomographic optical system with CT for intrinsically co-registered imaging. *Phys Med Biol*. 2010;55(6):1591-1606. doi:10.1088/0031-9155/55/6/004
26. Möller T, Trumbore B. Fast minimum storage ray-triangle intersection. *J Graphics Tools*. 1997;2(1):21-28. doi:10.1080/10867651.1997.10487468
27. Dehghani H, Guggenheim JA, Taylor SL, Xu X, Wang KK. Quantitative bioluminescence tomography using spectral derivative data. *Biomed Opt Express*. 2018;9(9):4163-4174. doi:10.1364/BOE.9.004163
28. Dehghani H, Eames ME, Yalavarthy PK, et al. Near infrared optical tomography using NIRFAST: algorithm for numerical model and image reconstruction. *Commun Numer Methods Eng*. 2008;25(6):711-732. doi:10.1002/cnm.1162
29. IVIS spectrum in vivo imaging system, Perkin Elmer Inc., Waltham MA. https://www.perkinelmer.com/product/ivis-instrument-spectrum-120v-andor-c-124262
30. Ami HTX Imaging System, Spectral Instuments Imaging, Tucson, AZ. https://spectralinvivo.com/imaging-systems/
31. Deng Z, Xu X, Dehghani H, et al. In vivo bioluminescence tomography-guided radiation research platform for pancreatic cancer: an initial study using subcutaneous and orthotopic pancreatic tumor models. *Proc SPIE* 2020;11224(9):1122409. doi:10.1117/12.2546503
32. Weersink RA, Ansell S, Wang A, et al. Integration of optical imaging with a small animal irradiator. *Med Phys*. 2014;41(10):102701. doi:10.1118/1.4894730
33. Zhang B, Wong JW, Iordachita II, et al. Evaluation of on- and off-line bioluminescence tomography system for focal irradiation guidance. *Radiat Res*. 2016;186(6):592-601. doi:10.1667/RR14423.1
34. Yu J, Zhang B, Iordachita I, et al. Systematic study of target localization for bioluminescence tomography guided radiation therapy. *Med Phys*. 2016;43(5):2619-2629. doi:10.1118/1.4947481
35. Ntziachristos V, Schellenberger EA, Ripoll J, et al. Visualization of antitumor treatment by means of fluorescence molecular tomography with an annexin V-Cy5.5 conjugate. *Proc Natl Acad Sci USA*. 2004;101(33):12294-12299. doi:10.1073/pnas.0401137101
36. Zacharakis G, Kambara H, Shih H, et al. Volumetric tomography of fluorescent proteins through small animals in vivo. *Proc Natl Acad Sci USA*. 2005;102(51):18252-18257. doi:10.1073/pnas.0504628102
37. Zilberman Y, Kallai I, Gafni Y, et al. Fluorescence molecular tomography enables in vivo visualization and quantification of nonunion fracture repair induced by genetically engineered mesenchymal stem cells. *J Orthop Res*. 2008;26(4):522-530. doi:10.1002/jor.20518

38. Bentley A, Xu X, Deng Z, et al. Quantitative molecular bioluminescence tomography. *J Biomed Opt*. 2022;27(6):066004. doi:10.1117/1.JBO.27.6.066004

SUPPORTING INFORMATION

Additional supporting information can be found online in the Supporting Information section at the end of this article.

How to cite this article: Xu X, Deng Z, Sforza D, et al. Characterization of a commercial bioluminescence tomography-guided system for pre-clinical radiation research. *Med Phys*. 2023;1-21. https://doi.org/10.1002/mp.16669